Chapter-6

Oxide Ion Conduction in Alkaline Earth Metal Doped Y_3GaO_6: Substitution on A Site

Pragati Singh, *Raghvendra Pandey, Tadeusz Miruszewski, Kacper Dzierzgowski, Aleksandra Mielewczyk-Gryn, Prabhakar Singh,* **“***Signature of oxide ion conduction in alkaline earth metal doped* Y_3GaO_6*’’, ACS Omega, 2020, 5,30395-30404.*

Pragati Singh, *Raghvendra Pandey, Tadeusz Miruszewski, Kacper Dzierzgowski, Aleksandra Mielewczyk-Gryn, Prabhakar Singh,* **“***Examine the consequences of calcium substitution on the structural and electrical properties of* Y_3GaO_6*’’,* **(***Revision Submitted)*

CHAPTER 6: Oxide-ion conduction in alkaline earth metal doped Y_3GaO_6: Substitution on A site

6.1 Introduction

In the continuation of the previous chapters, Y_3GaO_6 system was chosen as the second possible class of the electrolyte material. A recent report using first principle calculations has predicted that Ln_3GaO_6 (Ln = La, Nd, Gd, Tb, Ho, Dy, Er, or Lu) system could be a good oxide ion-conductor[29]. Earlier, a few experimental studies on some derivatives of these species have also been carried out by the researchers. To explore a new family of oxide ion conductors, we examined the bond valence energy landscapes (BVEL) of O^{2-} ions diffusion in a few yttrium containing oxide materials [112][141] and the BV based energy barrier for Y_3GaO_6 was found to be ~ 0.54 eV along the c-axis of the crystal structure. Hence, due to less energy barrier in Y_3GaO_6 than the other Y-containing oxide systems, this system was taken for further study. Till now, apart from structural studies, only a few optical studies like the luminescence behaviour of tri-yttrium gallate (Y_3GaO_6) have been reported.

In the present chapter, we have tried to investigate the physical properties of undoped and alkaline earth metal substituted Y_3GaO_6 systems. Here, divalent ions such as Ca^{2+}, Sr^{2+} and Ba^{2+} were doped on the *A*-site (i.e. *Y*-site), and their effect on the bulk electrical conductivity has been studied. This study aimed to explore alkaline earth metal doped Y_3GaO_6 as an oxide ion-conducting material and identify a suitable dopant for enhanced conductivity. This chapter is divided into two parts: in part A, Y_3GaO_6 is taken as the base material, and the effect of 2% alkaline earth metal doping on the Y site has been studied in detail. The compositions $Y_{(3-0.06)}M_{0.06}GaO_{6-\delta}$ (M = Ca^{2+}, Sr^{2+}& Ba^{2+}) has been synthesized by varying M, and the effect of alkaline earth metal on the physical properties in the above matrix has been explored. In part B, the influence of higher doping concentration of Ca on A-site has been investigated in detail. For this, we have synthesized the matrix $Y_{3(1-x)}Ca_{3x}GaO_6$ (x = 0, 0.02, 0.04, 0.08, 0.12), and the influence of higher dopant concentration of Ca on Ysite of the matrix has been investigated.

6.2 Experimental Procedure

Polycrystalline samples of Y_3GaO_6 and 2% Ca^{2+}-, Sr^{2+}-, Ba^{2+}- doped-Y_3GaO_6 were prepared via solid-state reaction route. The Y_2O_3 (otto, 99.99%), $CaCO_3$ (Alfa Aesar, 99.5%), $SrCO_3$ (Loba Chemie, 99.9%), $BaCO_3$ (Alfa Aesar, 99.9%)and Ga_2O_3 (Alfa Aesar, 99.99%), were preheated at 300 °C for 5h and weighed in stoichiometric amount. Details of the experimental procedures were already reported in chapter 2.

The structural study was done by Rigaku Miniflex-II desktop X-ray Diffractometer with Cu-$K_{\alpha1}$ radiation in the 2θ range of 10-120° and at the scan rate of 5°/min. The bulk density was calculated using the Archimedes density measurement kit (DENVER SI-234). Surface morphology and composition analysis of polished samples were carried out using SEM (EVO-Scanning electron microscope MA15 /18). Impedance measurement was carried out on the sintered pellet in the ambient atmosphere via Wayne Kerr 6500P series LCR meter using the two probe method. Data was collected in the temperature range of 400–700 °C using Platinum paste as the electrode. The total conductivity in a function of oxygen partial pressure was measured using a conventional DC-2W method using Keysight 34970 A precise digital multimeter with a data acquisition mode. The measurements were done in a temperature range of 650-800 °C. A gas mixer was used to introduce the proper atmosphere to the measurement cell. The atmospheres were changed from pure and dry argon to dry oxygen, and the step was 0.1 atm. During the measurements, samples were held at the final temperature to see the constant value of recorded resistance what indicated the thermodynamic equilibrium between the sample and gas. This procedure was repeated in every temperature and atmosphere. UV-Visible absorption spectra in the wavelength range of 200-1000 nm were recorded using JASCO V-770 UV–Vis spectrometer. Room temperature photoluminescence measurement was done using a photoluminescence spectrometer (FLOUROLOG HORIBA SCIENTIFIC) employing the excitation wavelength of 260 nm. Fourier Transform Infrared spectra were recorded using Nicolet iS5 THERMO Electron Scientific Instruments LLC in the wavenumber range of 400 - 4000 cm^{-1} using KBr media. Thermogravimetric analysis of the sample was done in the nitrogen atmosphere using Netzsch Jupiter®449 F1 (Burlington, MA, USA) with the gas flow rate of 100 ml/min. Thermal expansion of bulk sample in the temperature range of 50-1000 °C was studied using Netzsch DIL 420 PC/4 dilatometer with a constant cooling and heating rate of 2 °C/min in air flow. The thermal expansion coefficient is calculated by linear fitting the elongation vs temperature function.

To inspect the oxide ion diffusion path and migration barrier in the crystal structure, we have done bond valance-based energy calculations using soft-BV program[141]. The room temperature X-ray Rietveld refined crystallographic information file parameters were used for the bond valance energy calculations, and the BVE landscape and crystal structure were drawn using Vesta software[142]. The spatial resolution in the calculation was set to 0.1 Å. The energy barriers for oxide ion migration were estimated using the BVE landscape.

PART A

Oxide Ion Conduction in Alkaline Earth Metal Doped Y_3GaO_6

In this section, alkaline earth metal incorporated Y_3GaO_6 systems has been investigated in detail. We have substituted 2% of -Ca^{2+}, -Sr^{2+}, & -Ba^{2+}at the A-site of $Y_{(3-0.06)}M_{0.06}GaO_{6-\delta}$system. Hereafter, the undoped Y_3GaO_6 and 2% of -Ca^{2+}, -Sr^{2+}, -Ba^{2+} doped Y_3GaO_6 are abbreviated as YGO, YCGO, YSGO, and YBGO, respectively.

6.3 Results and Discussion

6.3.1 Structural Analysis

Comparative X-ray diffraction patterns of the YGO, YCGO, YSGO and YBGO samples in the 2θ ~ 10°-120° are shown in Fig. 6.1 (a). All the diffraction peaks are found to be phase pure and indexed according to the non-centrosymmetric orthorhombic symmetry with space group $Cmc2_1$. The X-ray diffraction patterns of all the compositions match with the standard ICSD file No. 155086. The polyhedral representation of the YGO system is shown in Fig. 6.1 (b), representing a similar crystal structure as earlier reported in the literature [113]. The Rietveld refinements were carried out using Fullprof software taking Pseudo-Voigt peak profile (Fig. 6.2) [206]. The atomic coordinates were allowed to vary free of constraints, and the values obtained in each stage were used as a starting parameter for further refinements. The occupancy factor for all the elements was kept fixed to their nominal value. The value of lattice parameters calculated from refinement are listed in Table 6.1. The ions Y, Ga, and O occupy *8b* & *4a*, *4a,* and two *8b* + two *4a* Wyckoff positions, respectively. The coordination no. of Y, Ga, O atoms was found to be 7, 4 & 4, respectively, in the YGO system. After di-valent doping on Y^{3+} site, there is a slight increase in the volume as Ca^{2+} (1.20Å), Sr^{2+} (1.35Å) & Ba^{2+} (1.52Å) have larger cell volume as compared to Y^{3+} (1.10Å)[207]. It is easier to introduce lesser amount of Ca into the Y_3GaO_6 lattice without causing a major lattice distortion. As the doping level of Ca further increases, a secondary phase of Y_2O_3 corresponding to JCPDF NO. 89-5591 is found to evolve. This indicates that the solid solubility limit of the divalent atom is only ~2-3%. However, for the other substituent as Sr^{2+} and Ba^{2+}, it is expected that the dissolution limit is less at Y-site, and also, they will create much distortion in the lattice in comparison to Ca^{2+} because of larger mismatch of ionic radii between the host and dopants ions.

Table 6.1: Rietveld refined lattice parameters, volume, density and porosity of the studied compositions

Sample	**Phase**	**Lattice Parameters**			**Volume**	**Relative**	**Porosity**
		a (Å)	**b(Å)**	**c(Å)**	**(Å^3)**	**Density**	
YGO	Orthorhombic (*Cmc*2$_1$)	8.843(1)	11.098(1)	5.398(1)	529.765	69.98 %	0.300
YCGO	Orthorhombic (*Cmc*2$_1$)	8.845(3)	11.101(6)	5.396(9)	529.970	97.61 %	0.024
YSGO	Orthorhombic (*Cmc*2$_1$)	8.849(5)	11.107(1)	5.398(2)	530.599	97.61 %	0.024
YBGO	Orthorhombic (*Cmc*2$_1$)	8.844(4)	11.099(6)	5.401(1)	530.226	88.40 %	0.116

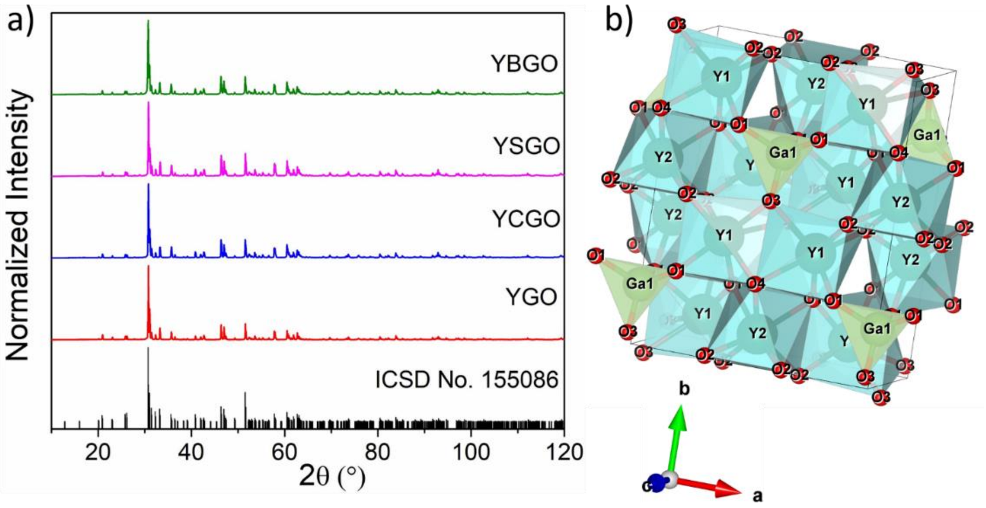

Figure 6.1: (a) Room-temperature XRD pattern of the studied samples and XRD of Y_3GaO_6 taken from ICSD database **(b)** 3D polyhedral representation of crystal structure

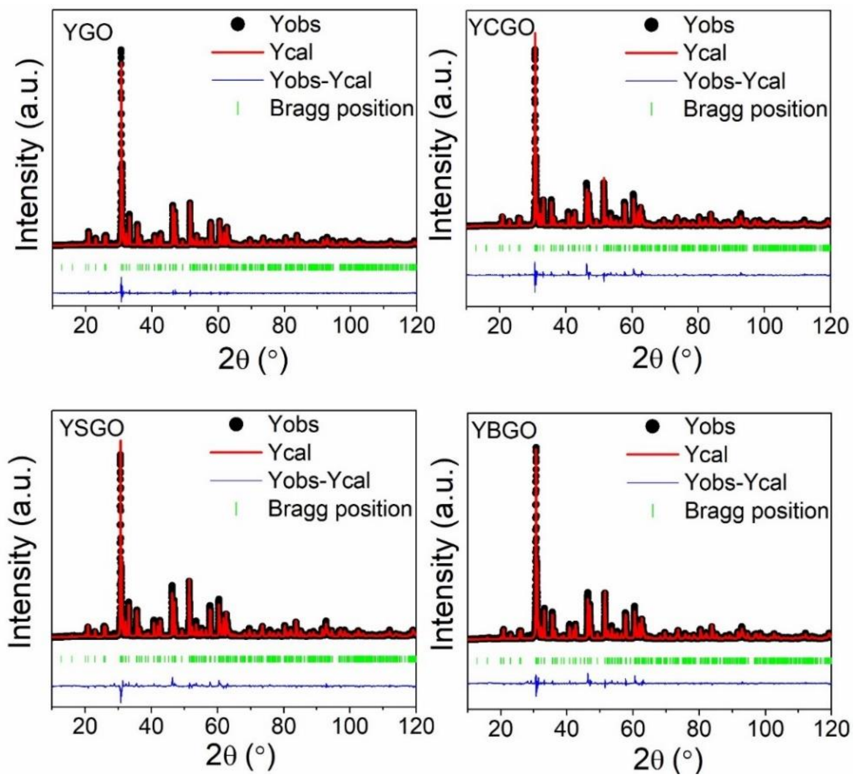

Figure 6.2: Rietveld refined patterns with observed (black circles), calculated (solid red line), Bragg reflections (green vertical ticks) and (blue line) difference profiles for the studied compositions sintered at 1350 ˚C for 6h

Bond Valance Energy-Based Approach for identification of migration pathways:

The Bond Valence model is an imperative approach to evaluate the chemical credibility of inorganic crystal structures. This model is based on the bond-valence sum *(BVS)* rule from Pauling's electrostatic valence concept, which expresses that the sum of all bond valences linked to an atom almost equals the absolute value of its oxidation state. According to this approach, the sum of bond valences, S_{ij}, about any ion, i, is equal to its valence, V_i (i.e. the formal oxidation state)

$$V_i = \sum_j S_{ij} \tag{6.1}$$

where the sum runs over all adjacent atoms j of the atom i. The bond valence S_{ij} can be considered as a measure of the electrostatic flux between a cation and an anion. It is directly related to the strength of the bond and is correlated inversely with bond length. It can be estimated by the following relation:

$$S_{ij} = exp\left(\frac{R_o - R_{ij}}{B}\right) \tag{6.2}$$

where R_o and B are constant parameters and R_{ij} is the interatomic distance between atoms i and j. For many bonds, B is approximated to 0.37. The Bond valence approach also explains the structural distortions from the ideal three-dimensional crystal structure by calculating the global instability index parameter [139][140]. Although the energy barriers obtained by BVS analysis are only relative and not as accurate as the ones obtained by more sophisticated computational methods. To explore a new family of oxide ion conductor, we examined the bond valence energy landscapes (BVEL) of O^{2-} ions diffusion in a few yttrium containing oxide materials [112][141]. Using BVE approach, the BV based energy barrier for Y_3GaO_6 was found to ~ 0.54 eV along the c-axis of the crystal structure. Hence due to less energy barrier in compared to other Y containing oxide systems, this system was taken for further study. Figure 6.3 (a) shows the schematic bond valance energy (BVE) landscape for the migration of a single oxygen ion inside the crystal. The volumetric data in the *cube file* generated through Soft-BV using a crystallographic information file can be directly visualized to recognize low energy-barrier migration pathways. Moreover, through this approach, the equilibrium & interstitial sites and their connectivity through transition states can be recognized without any kind of intervention. The purpose of this approach is to identify voxels in the energy landscape, which are local minima or saddle points and then to connect them by tracing from saddle-point voxels to minima voxels. Figure 6.3 (b) shows the crystal structure along with the 3D view along with the iso-surface (energy value at 2.7 eV). Connection of iso-surface means the existence of low energy barrier for the oxide ion migration and no connection on the iso-surface suggests difficulty for the oxide ion to migrate across the barrier [193][208].

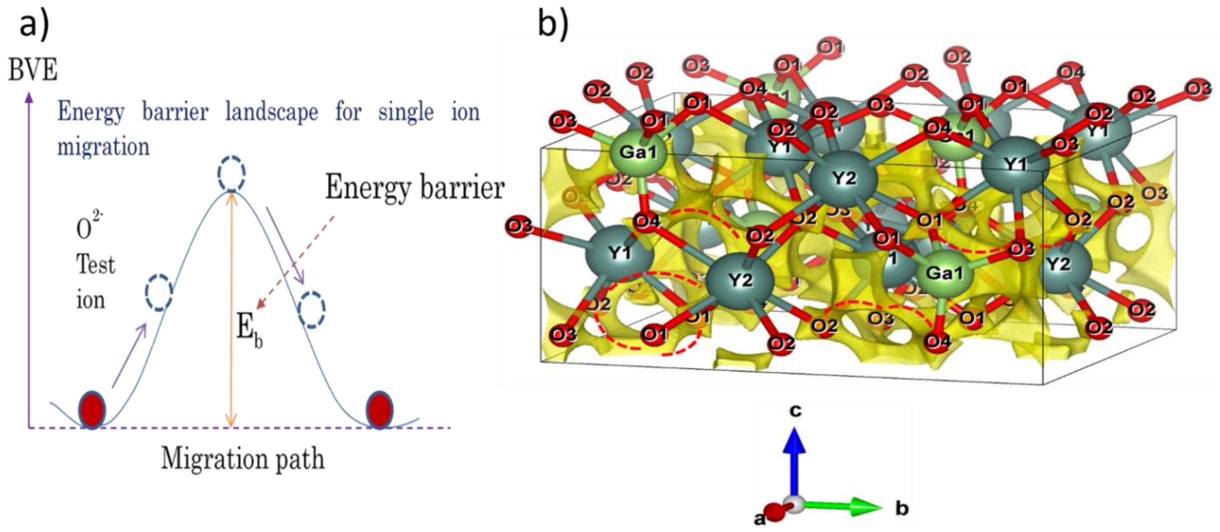

Figure 6.3: (a) Schematic of the energy barrier landscape of single oxide ion migration inside the crystal lattice. **(b)** Crystal structure, including migration iso-surface of at 2.7 eV in Y_3GaO_6. Yellow colour represents the iso-surface. Connection of yellow iso-surface represents the possible oxide ion migration path. Dotted red lines are shown for the aid of visualisation

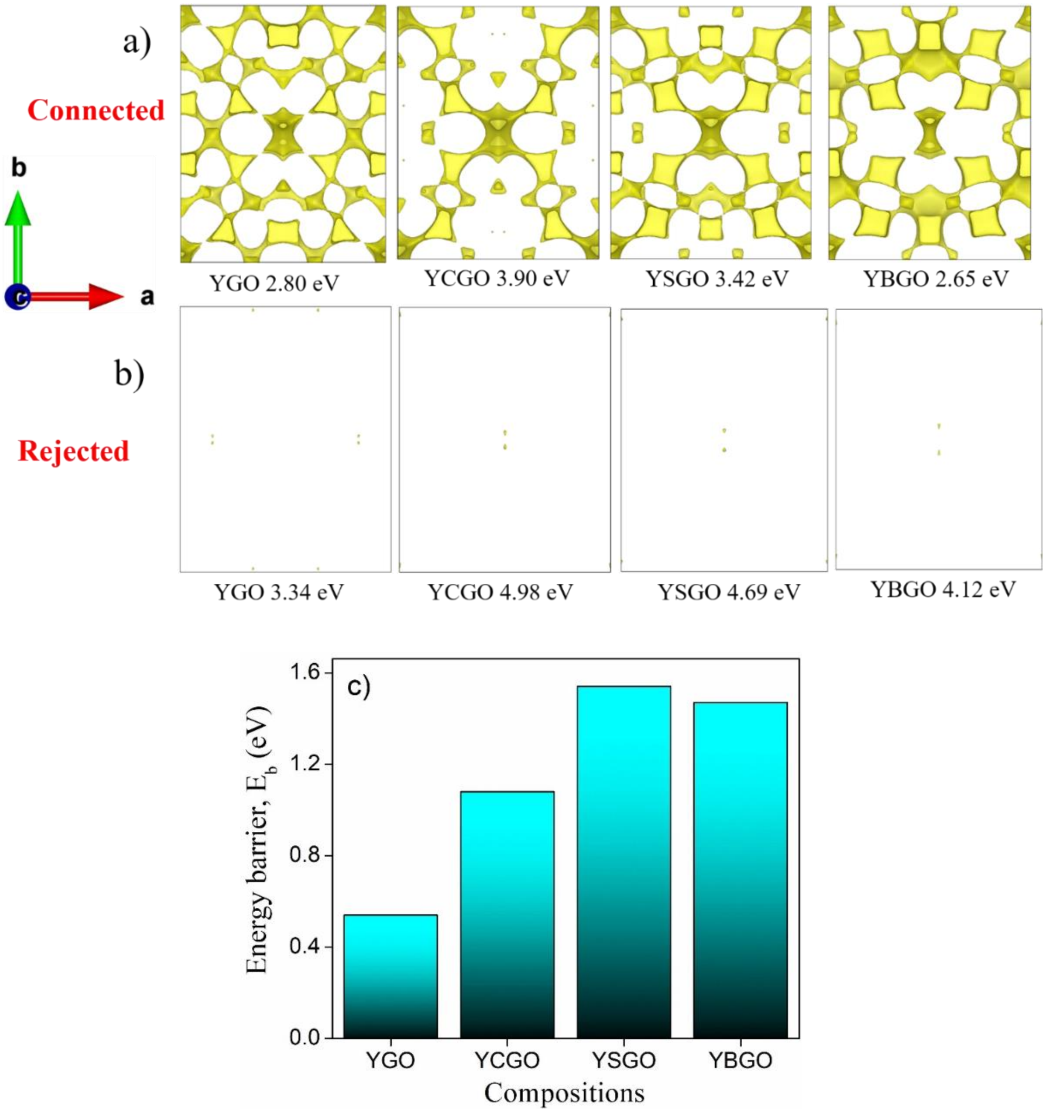

Figure 6.4: (a-b) Bond valance energy landscape for oxide ion migration viewed along c axis with various iso-surface. Yellow iso-surface in Fig. (a) represents the presence of migration pathway, and the rejected iso-surface in Fig. (b) represents the absence of migration channel. The energy difference between fig. a and b gives the Energy barrier E_b for migration at room temperature (c) Energy barrier histogram at room temperature for studied compositions. Despite of the increase in the oxygen vacancies with aliovalent doping, doped compositions are showing higher energy barriers. This may be due to the high association energy of dopants and defects formed

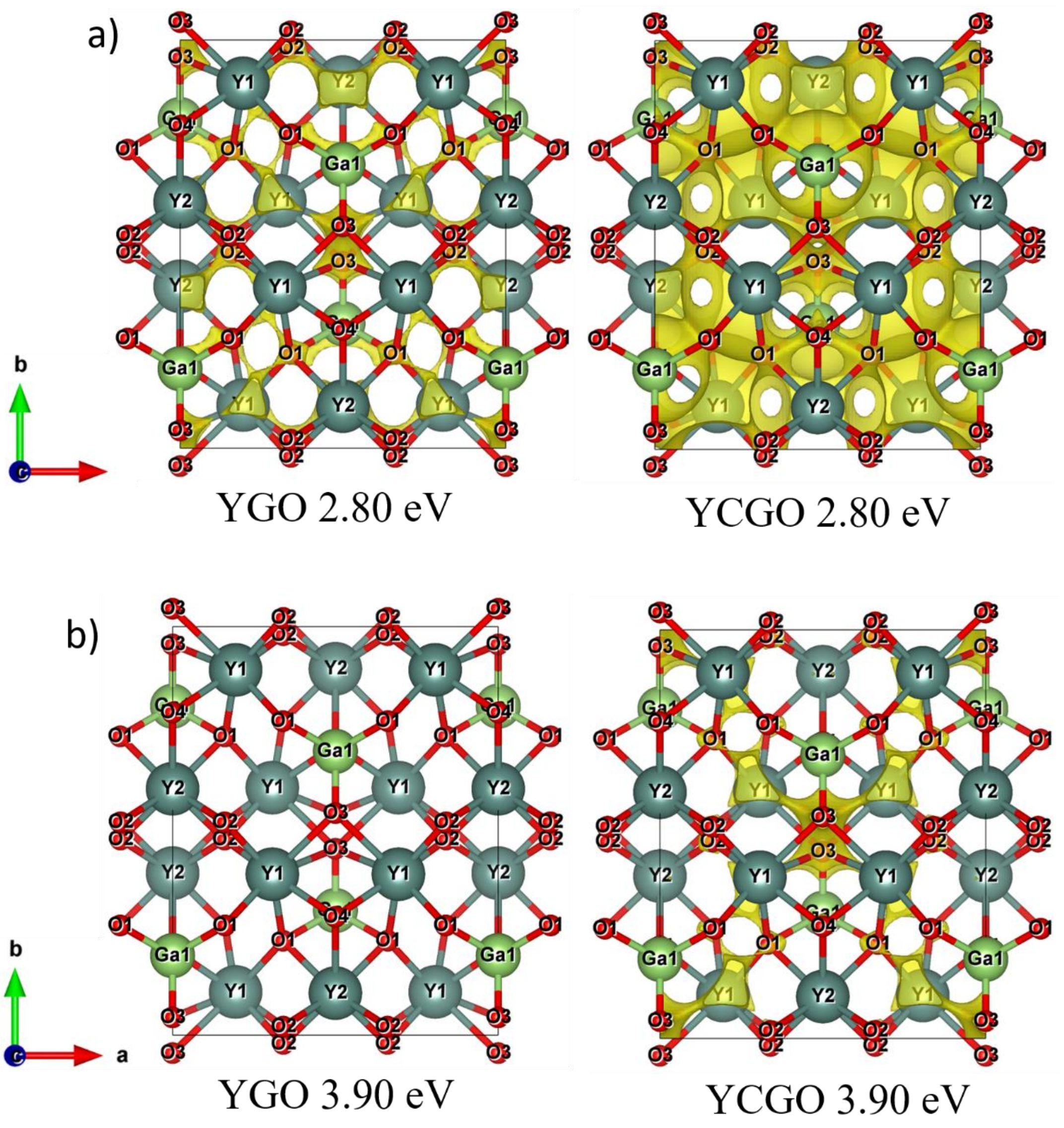

YGO 2.80 eV

YCGO 2.80 eV

YGO 3.90 eV

YCGO 3.90 eV

Figure 6.5: Oxygen ion diffusion iso-surface channel of YGO and YCGO along *c*-axis at **(a)** 2.80 eV **(b)** at 3.90 eV derived from the bond valence energy landscape using VESTA software. At an iso-surface value of 3.90 eV, the migration pathways are observed for YCGO sample, whereas at the same value no any connected path is observed for YGO sample

The migration pathways in the BVE calculations were constructed with linearly interpolated images between the fully relaxed starting and ending structures. The energy barrier for oxygen migration is calculated as $E_a = E_{max}-E_{min}$, where E_{max} and E_{min} are the highest and the lowest energy along the migration pathway, respectively (Fig. 6.4). Figure 6.3 (b) and 6.5 (b) show BV based energy landscapes for an oxide ion in YGO and YCGO at the iso-surface value of (a) +2.80 eV (b) +3.90 eV, respectively, where the BV-based energy of the most stable position is set to 0 eV. The yellow iso-surface of the BV-based energy of YGO did not connect across the unit cell (Figure 6.5 (b)), indicating relatively difficult anion migration. On the contrary, we found that YCGO had the highest connecting pathways for oxide-ion migration across the unit cell. BV-based energy landscapes indicate that an oxide ion can migrate along the edges of GaO_4 tetrahedra and corners of the YO_7 polyhedra. Figure 6.3 (b) & 6.4 shows that the possible oxide-ion diffusion pathways in the [010] direction are via -O3-O3-O3-O1- and thru the interstitials. From the reaction coordinates, it is evident that the YGCO has no intermediate pathway segment between -O3-O3- migrations while other compositions have pathway segments for migration. This may be a probable cause to ease the migration of O^{2-} ions across vacant oxygen sites within the YCGO crystal structure. Though, all the crystallographic information and studies presented here are based on room temperature XRD studies of the compositions. The BV-based energy barriers for oxide-ion migration along visualization axes *a*, *b*, and *c* directions were estimated and found to be minimum along the *c* direction. Therefore, it is expected that YCGO exhibit one, two- or three-dimensional oxide-ion diffusion and relatively easier migration than that of the other studied compositions.

6.3.2 ConductivityAnalysis

The complex impedance plot of all the studied samples at 600 °C are shown in Fig. 6.6(a). YGO and YBGO samples were found to exhibit a single depressed semi-circular arc, whereas YCGO and YSGO samples exhibit two semi-circular arcs. No apparent electrode response is observed for any of the samples due to the frequency limit of the instrument. The centre of all the semi-circles are lying below X-axis shows the presence of Non-Debye type relaxation behaviour. The semi-circular arcs are modelled with the equivalent circuit, and the contribution of each part is distinguished with the help of corresponding circuit model. The equivalent circuit used to fit the data consists of two series R-CPE elements associated with bulk and grain-boundary contribution (shown in the inset of Fig. 6.6 (a) and (b)). The capacitance related to all contributions are calculated according to the following relation: $\omega = \frac{1}{RC}$, where ω is the relaxation frequency, R is the resistance, and C is indicative of bulk response. The capacitance values of bulk and grain boundary at 600 ºC are listed in Table 6.2. The lower value of CPE in the higher frequency range is the effect of bulk material, and the higher capacitance value at the lower frequency range is because of the grain-boundary contribution.

Table 6.2: Value of grain, grain-boundary capacitance, total conductivity at 600 ºC, and activation energy of studied compositions

Composition	**C_b (F)**	**C_{gb} (F)**	**σ_{total} (Scm^{-1}) at 600 ºC**	**Activation energy (eV)**
YGO	0.24×10^{-12}	0.11×10^{-9}	0.953×10^{-7}	1.361
YCGO	1.62×10^{-9}	4.14×10^{-6}	0.572×10^{-4}	0.686
YSGO	3.66×10^{-9}	8.70×10^{-6}	0.180×10^{-4}	0.918
YBGO	0.19×10^{-10}	0.29×10^{-9}	0.122×10^{-6}	0.973

The resistance of bulk and grain-boundary are calculated from the intercept of the corresponding arc on the real axis (Z´). The total resistance of the electrolyte is given by: $R_t = R_b + R_{gb}$, where R_b is the bulk resistance and R_{gb} is the grain-boundary resistance. Further, this total resistance of the electrolyte was used to obtain the total conductivity using the formula: $\sigma_t = \frac{d}{AR_t}$ where, σ_t is the total conductivity, R_t is the total resistance, d is the thickness, and A is the area of the pellet. The temperature dependence of total conductivity of all the samples are shown in Fig 6.6(c). It is remarkable that the conductivity increases significantly for the Ca^{2+} and Sr^{2+} dopant, while it gets declined for Ba^{2+} dopant. Figure 6.6(c) depicts the Arrhenius representation of the conductivity data. The activation energy (E_a) is estimated for the studied compositions using the Arrhenius equation:

$$\sigma T = \sigma_0 \exp\left(\frac{-E_a}{k_B T}\right) \tag{6.3}$$

where, σ_0 is the preexponential factor, k_B Boltzmann's constant, and E_a is the activation energy. The activation energy has been calculated by the slope of the Arrhenius plot, which is in good agreement with a few other earlier reported prominent anionic conductors [209]–[211], indicating the formation of vacancies and ionic charge carriers. The activation energy (E_a) is equal to the sum of the vacancy formation energy (E_f) and the migration barrier (E_m). The E_m depends on the local atomic arrangement of the system. In this study, E_m, obtained from the BVE approach, is the minimum for YCGO composition among all the doped compositions. Hence, the activation energy is minimum for the YCGO sample. The bulk conductivity of 2 % of Ca doped sample (YCGO) was found to be a maximum due to minimal mismatch of ionic radii to the host atom and comparatively less dissociation energy in the Ca-O bond (Table 6.3). The highest solubility limit in $Y_{2.94}Ca_{0.06}GaO_{6-\delta}$ can be attributed to the smallest size mismatch[212] for Ca^{2+}, $|r(Ca^{2+}) - r(Y^{3+})| < |r(Sr^{2+}) - r(Y^{3+})| < |r(Ba^{2+}) - r(Y^{3+})| = 0.06 < 0.19 < 0.21$ Å. Here the $r(A)$ denotes the ionic radius of A^{2+} cation. This leads to less activation energy of migration in the YCGO sample in comparison to others. At higher temperatures, the no. of vacancies will be dissociated; hence the ionic conductivity is directly related to the formation of oxygen vacancies.

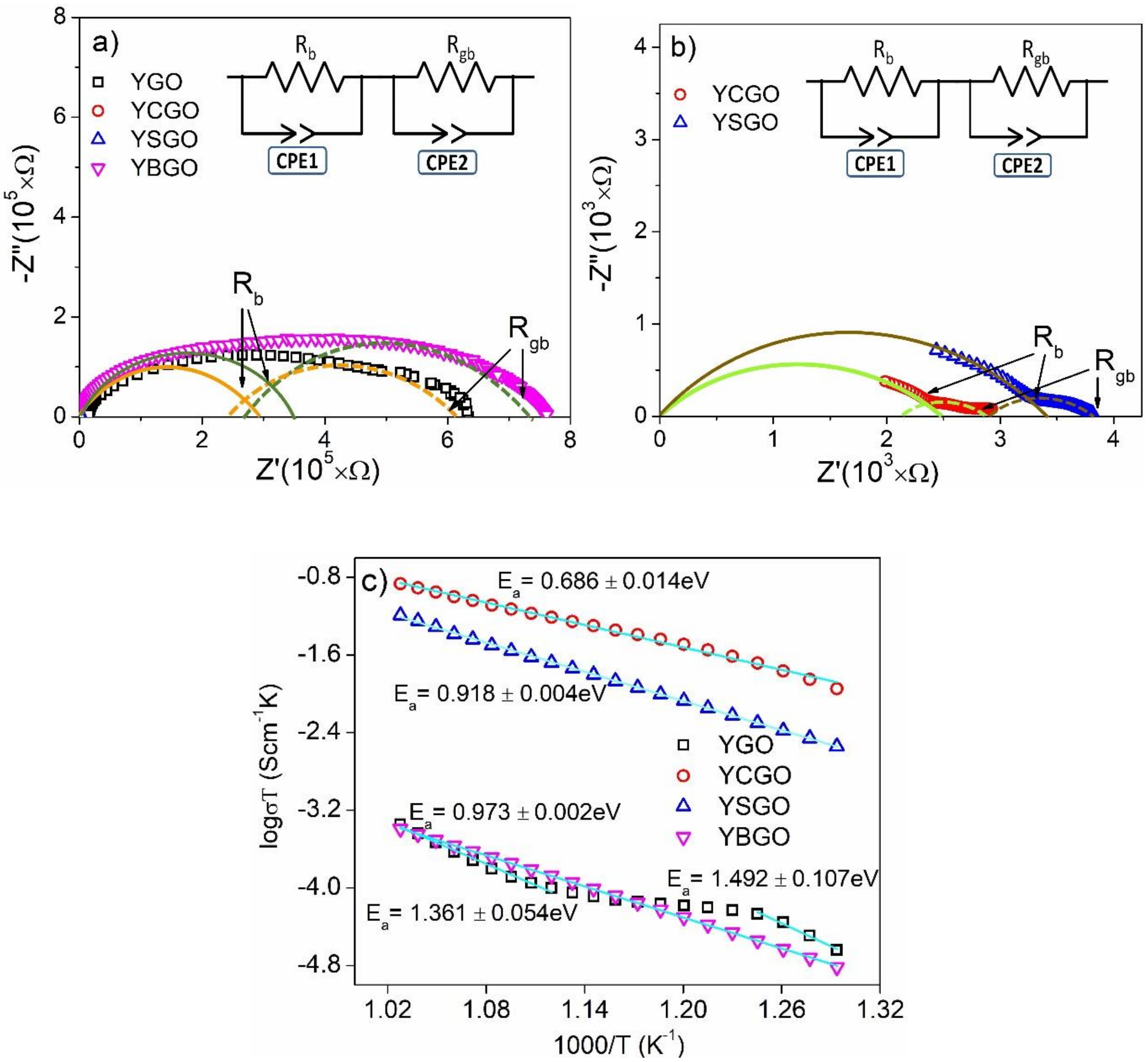

Figure 6.6: (a) Complex Impedance plot of studied compositions at 600 °C in the air. Hollow symbol and line represent experimental data and equivalent circuit fit, respectively. Inset in the figure represents the corresponding equivalent circuit used to fit the spectra. The solid arc in fitting represents bulk contribution, and the dotted arc represents grain boundary contribution. R denotes resistance, and CPE represents the constant phase element **(b)** Complex Impedance plot for YCGO and YSGO sample. Symbol and line represent experimental data and fit, respectively. Inset in the figure represents the equivalent circuit used for fitting. **(c)** Arrhenius plot (Variation of log [σ_{bulk}*T] with the inverse of temperature) of the studied compositions with the inversed of temperature. Cyan line shows the linear fit, and the number are the calculated activation energies

Table 6.3: Bonding strength with the oxygen of di-valent *A*-site dopant[213]

Bond	Bond Dissociation Energy (kJ/mol)
Y-O	~715
Ca-O	~464
Sr-O	~454
Ba-O	~454

Effect of Dopant Size and Conductivity as a function of oxygen partial pressure

For fixed valency substitution and a fixed number of vacancies, conductivity depends on the dopant size. Total conductivity variation against the ratio of dopant radii and host radii is shown in Fig. 6.7(a). The maximum conductivity is obtained for Ca^{2+} doping with $r_{Ca^{2+}}/r_{Y^{3+}}$ ~1.09. These types of optimum values are observed in many other ionic conductors such as $NdGaO_3$, $LaAlO_3$, $BaGdInO_4$, $La_{9.33}X_{0.67}Si_6O_{26}$, $Na_{0.5}Bi_{0.5}TiO_3$[214]–[219]. It is believed that the maximum conductivity appears for the r_{dopant}/r_{host}~1.05 in the perovskite and brownmillerite type structure[215].

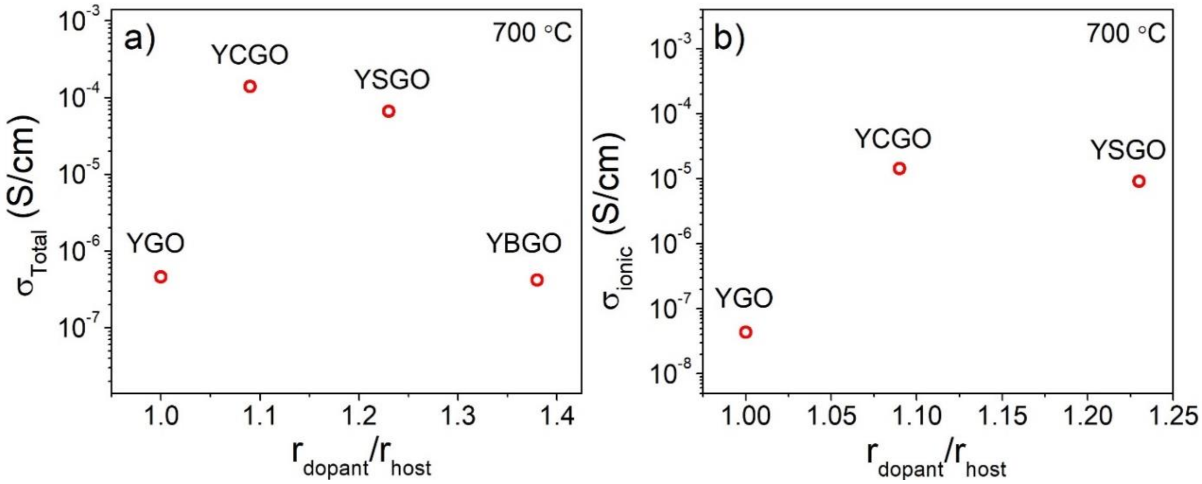

Figure 6.7: Dependence of **(a)** total conductivity **(b)** oxide ion conductivity on the dopant ionic radii at 700 °C

As the comparable size of dopant and host minimizes the local strain in the lattice and assists the migration of oxygen ions (shown in Fig. 6.8)[215]. Total conductivity as a function of oxygen partial pressure at 700 °C and 800 °C is shown in figure 6.9. The flat region at a lower partial pressure in all the studied samples is attributed to predominant ionic contribution and the positive slope of the curve at $pO_2 > 10^{-4}$ atm, showing p-type conduction with a predominant hole conductivity. The extent of ionic contribution is changing with the substitution and temperature. As the hole and electron, concentrations increase rapidly with the increase in the temperature, the mobility of oxide ions decreases [220]. The process of hole formation can be described by the equation:

$$V_O^{\cdot\cdot} + \frac{1}{2}O_2 \leftrightarrows O_O^X + 2h^{\cdot} \tag{6.4}$$

Thus, the total conductivity will be given by

$$\sigma_{total} = \sigma_p \sim {V_O^{\cdot\cdot}}^{1/2} P(O_2)^{1/6} \tag{6.5}$$

where $V_O^{\cdot\cdot}$ is nearly constant and the slope of logσ vs log pO_2 is ~1/6 in higher partial pressure region. In the lower pO_2 region (< 10^{-4} atm), the concentration of oxygen vacancies is higher than the concentration of holes and electrons, and the total conductivity is given by

$$\sigma_{total} = \sigma_{V_O^{\cdot\cdot}} = constant \tag{6.6}$$

Since Y^{3+}, Ga^{3+}, Ca^{2+}, Sr^{2+}, and Ba^{2+} are neither prone to oxidation nor reduction so we can expect the conductivity to remain constant at lower partial pressure. Further, as the mobility of cationic species such as Y^{3+}, Ga^{3+}, Ca^{2+}, and Sr^{2+} are negligible, so we can conclude that the conductivity is mainly because of oxide ions in the given range of oxygen partial pressure. The variation of ionic conductivity with the dopant size at 700 °C is shown in Fig. 6.7(b).

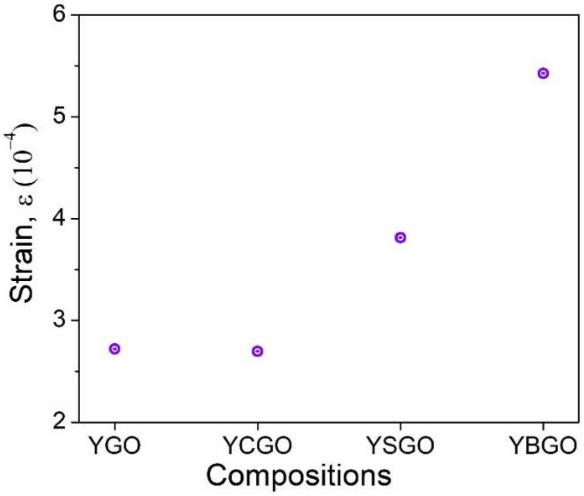

Figure 6.8: Intrinsic strain developed inside the crystal due to defects, grain boundary and faults calculated using Williamson-Hall analysis

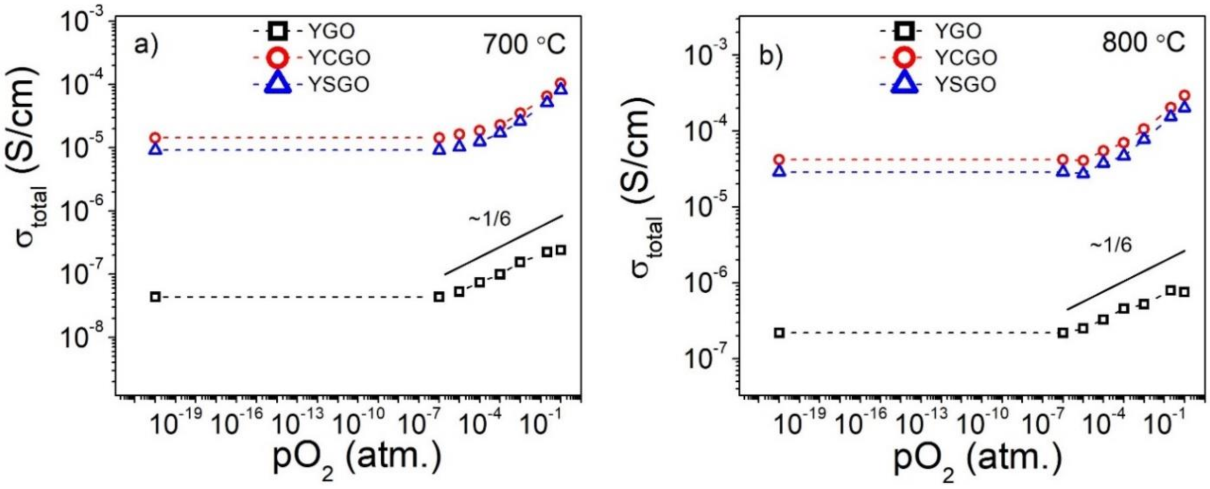

Figure 6.9: Oxygen partial-pressure dependence of total electrical conductivity of YGO, YCGO, and YSGO samples at **(a)** 700 and **(b)** 800 ˚C, respectively. It suggests dominant oxide-ion type conduction in the pressure range of 10^{-4}-10^{-20} atm

6.3.3 Photoluminesce (PL) Analysis

The photoluminescence spectra of the synthesized material in the wavelength range of 280-500 nm is shown in Fig. 6.10. The excitation wavelength of 260 nm is used within the 1 nm slit. A strong emission peak is observed at ~ 400 nm. Interaction of the electron-hole pair is analyzed using Photoluminescence spectra. The peak position of all the materials is same; however, intensity changes significantly after Ca and Sr doping. PL intensity changes due to the presence of defects associated with the doping. High intensity of pure YGO sample indicates high recombination rate of electron and hole pair. Usually, lower PL intensity corresponds to the higher conductivity because of the lower recombination rate and effective charge carrier separation[221]. Thus, the lower PL intensity of YCGO and YSGO sample confirms the formation of more oxygen vacancies and are correlated with the charge transfer between dopant and host ions. These results are as per the UV-vis and conductivity analysis. High PL intensity of YGO indicates its crystalline nature with lesser defects.

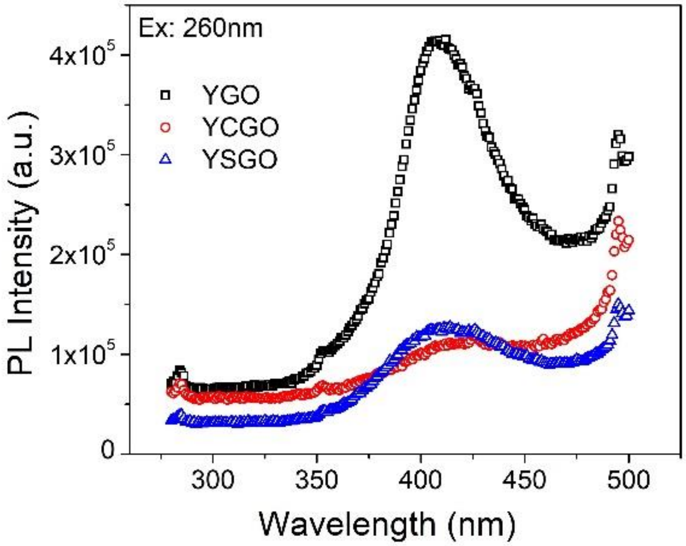

Figure 6.10: Room temperature photoluminescence spectra under an excitation wavelength of 260 nm and slit width 1nm

6.3.4 UV-Vis Analysis

Figure 6.11 depicts the band gap variation of the studied composition. The band gap of the studied compositions was calculated using Tauc's relation[222], represented by the relation:

$$\alpha h\upsilon = A(h\upsilon - E_g)^n \tag{6.7}$$

where A is constant, $h\upsilon$ is energy, α is absorption coefficient, E_g is band gap and n characterize the probability transition rate. n = 1/2 for direct transition n = 2 for indirect transition process. The observed direct band gap of pure YGO is found to be 5.49 eV, and its value is found to decrease with divalent doping. This decrease in band gap is accounted to increase in the oxygen vacancies formed by the charge compensation mechanism[223]. Among all the doped composition, Ca^{2+} have the lowest solution energy on Y^{3+} for creating oxygen defects. So, the number of defects formed will be maximum for Ca^{2+}. This type of behaviour is observed in $NdBaInO_4$[212]. Further, these results are also evident from the photoluminescence analysis. Its intensity is found to decrease with the dopant, with minima for Ca doping. This suggests that the vacancy concentration is maximum for Ca doping.

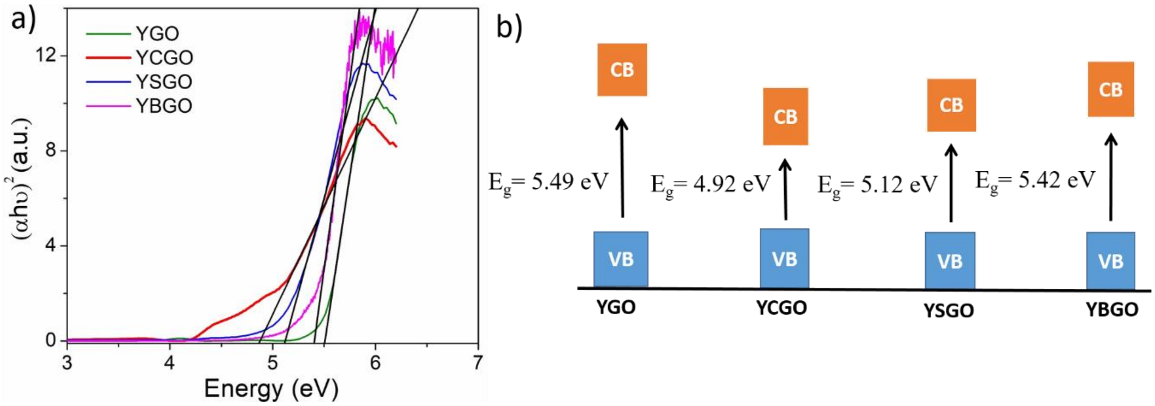

Figure 6.11 (a) Tauc's plot for direct band-gap calculation of YGO, YCGO, YSGO and YBGO samples. **(b)** Corresponding band structure.

6.3.5 FTIR Analysis

Fourier transform infrared technique is used to get information about the chemical bond and structure of the material. The bands are formed by bending and stretching of vibrations. The FTIR spectra of undoped and Ca^{2+}-, Sr^{2+}-, Ba^{2+}-doped YGO samples are shown in Fig. 6.12. The characteristic peak around 3400 cm^{-1} is assigned to the stretching vibrations of O-H associated with the hydroxyl group [224]. The peak around 1600 cm^{-1} is attributed to the H-O-H bending vibration. As the synthesized compositions did not contain any O-H molecule-based precursor, and XRD of the sample is also showing the clean phase. So, we can conclude that the OH peak observed in the spectrum is because of the moisture adsorbed on the powder sample during measurement. A strong band at 526-694 cm^{-1} is attributed to the stretching of the Y-O vibrations [225], and the band originated at 450, and 627 cm^{-1} is assigned to Ga-O vibrations, probably due to the formation of metal oxide bond. However, a slight decrease in the magnitude and peak broadening is observed after doping with alkali earth metal, mainly because of the increase in the defects and distortion caused by dopant ions in the host lattice [226]. The Ca-O peak appears around 300 – 400 cm^{-1} is not observed in the band. The presence of band around 2350 cm^{-1} in the YCGO sample can be attributed to the Ca-O bond [227]. Peak around 870 cm^{-1} presents in the YSGO sample is assigned to the Sr-O bond, and the kink around 860 cm^{-1} is assigned to Ba-O bond[228].

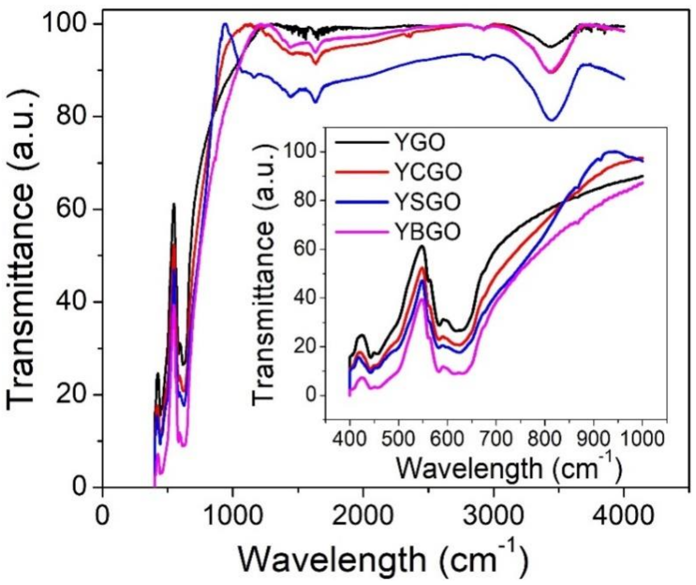

Figure 6.12: Room temperature FTIR spectra of YGO, YCGO, YSGO and YBGO samples. Figure in the inset shows the decrease in the metal-oxygen bond intensity with the increase in the atomic mass of dopant

6.3.6 SEM Analysis

SEM images of the fractured cross-section of YGO, YCGO and YSGO samples are shown in Fig. 6.13. Irregular and agglomerated grains for the YGO sample is attributed to the poor sinterability of the material. However, micrographs of the alkaline earth metal doped-YGO samples show quite dense & polygonal morphology with low porosity. The densification of the doped samples indicates the improvement in the sinterability after doping. Grains become more connected after doping, and the effective number of grain boundaries increases. The average grain size is calculated using image *J* software. Grain size is observed to increase with the doping of alkaline earth metal ions. The density of all the samples was calculated using the Archimedes principle. The density is found to increase with the alkaline earth doping [214][229], as summarized in Table 6.1. The increase in density is correlated with the increase in the grain size, as observed in the SEM micrographs of the sample.

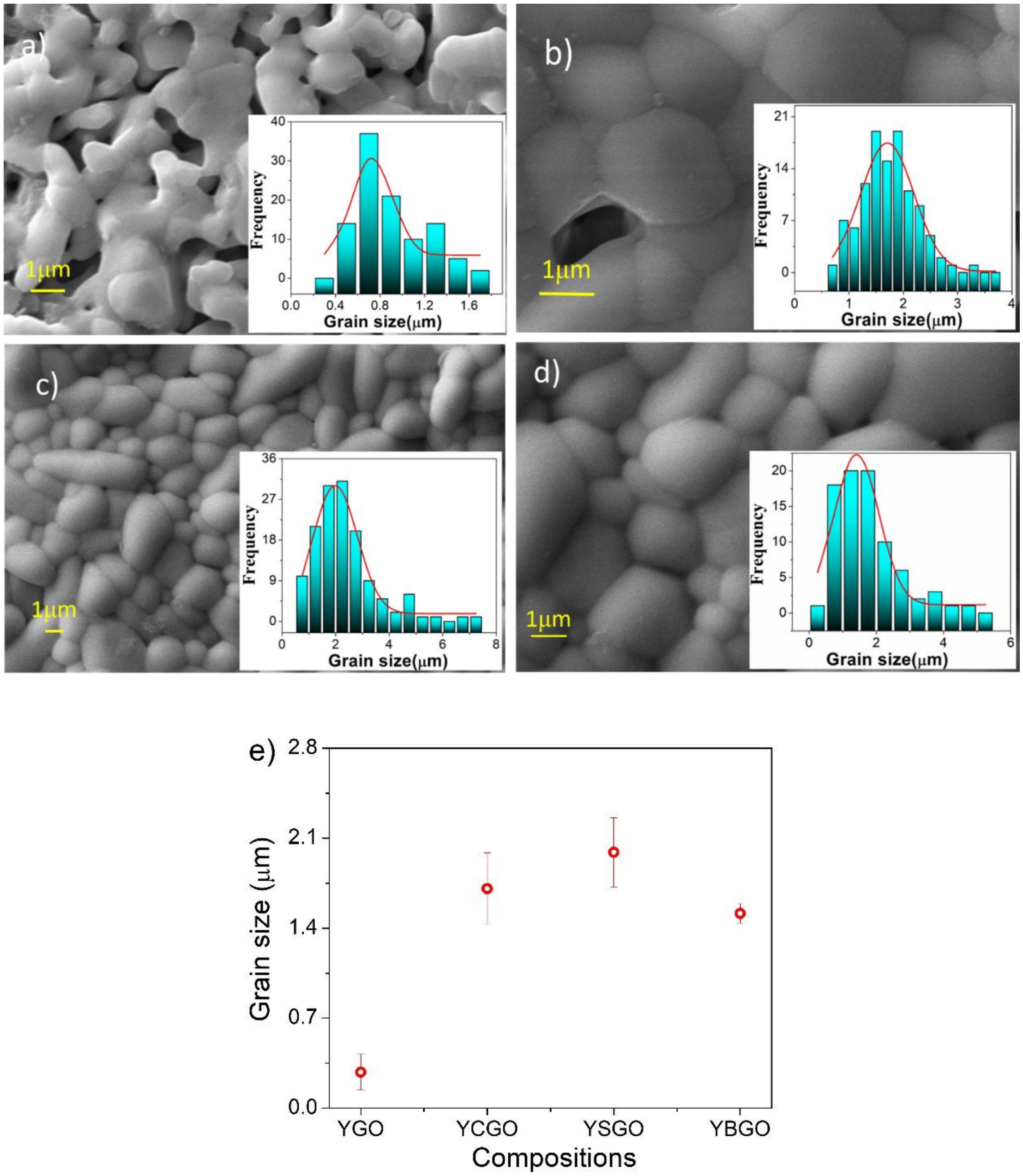

Figure 6.13: (a-d) SEM Micrographs of YGO, YCGO, YSGO and YBGO samples. Inset in the figure shows grain size distribution **(e)** Grain size variation of the studied compositions

6.3.7 Thermal Expansion Study

The variation of thermal expansion of pure YGO, and Ca^{2+}-, Sr^{2+}- doped-YGO are shown in Fig. 6.14. No appreciable difference is observed in the heating and cooling curve. All the samples show the linear change with temperature. This trend also indicates the absence of any kind of structural change in the studied temperature change. Thermal expansion coefficient can be obtained using the following relation:

$$\alpha_L = \frac{\Delta L}{L\,\Delta T} \tag{6.8}$$

where α_L denotes the value of thermal expansion coefficient (TEC), L is the length of sample ΔL is the change in length, and ΔT is the change in temperature[230].

TEC of all the samples are approximately the same. This indicates that the introduction of 2% of Ca^{2+} and Sr^{2+} doesn't change the TEC value. Its TEC values are close to lightly doped $La_{1-x}Sr_xMnO_3$, so it will exhibit better thermal compatibility with the $LaMnO_3$ family cathode materials. The obtained TEC values (mentioned in table 6.4) are also corroborated with TEC values of many manganite and nickelate based cathode materials as reported in the literature [231].

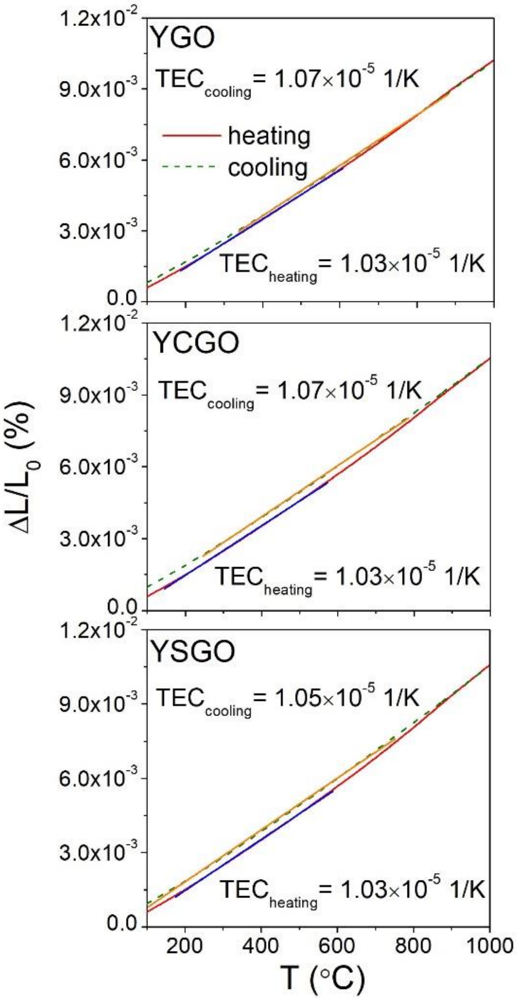

Figure 6.14: Thermal expansion curve of YGO, YCGO and YSGO compositions from Room temperature to 1000 ºC

Table 6.4: TEC of the measured sample between room temperature and 1000 ˚C

Compositions	**Thermal expansion coefficient α_L×10^{-6} (K^{-1})**
YGO	10.7
YCGO	10.7
YSGO	10.5
YBGO	---

6.4 Conclusion

Doping of small amount of Alkaline earth metal ion has a remarkable effect on the properties of Y_3GaO_6. Partially replacing the Y by 2% of Ca^{2+} or Sr^{2+} improves the bulk conductivity by more than three orders without any alteration in the conduction mechanism. However, the doping of Ba^{2+} didn't show any significant effect on the enhancement in the conductivity. Higher electrical conductivity with the Ca doping is attributed to the oxygen vacancies and the formation of migration channels only. Doping of alkaline earth metals in Y_3GaO_6 results in an increase in the conductivity and decrease in the band gap. Despite higher polarizability and lower bond strength of Sr^{2+} with O, the Ca^{2+} doping was found more effective and efficient than the Sr^{2+}. This is accounted to the optimum dopant size mismatch with the host ion as it produces minimum strain in the crystal lattice. The microstructures show an increase in grain size and densification after doping of alkaline earth metals. This is owing to the lower melting point of Ca^{2+}, Sr^{2+} and Ba^{2+} compared to Y^{3+}. The Bond valence energy-based approach was employed to screen and identify the oxide ion migration pathways in the crystal structure of the investigated compositions. Oxygen partial pressure dependence of total electrical conductivity (pO_2) study at 700 and 800 °C confirms that the material is oxide ionic conductor in the wide range of partial pressure (~ 10^{-20} – 10^{-4} atm). Furthermore, this system has the potential to improve its ionic conductivity on further optimizing the dopant and synthesis method. The other structural, microstructural (like SEM), Thermal (TEC, TGA) and optical characterizations (like PL, UV, FTIR) are also in support with the XRD, BVE and electrical behaviour and correlated with the experimental findings. Thus, this study explores a new family of anionic conductors that in future may be used in electrochemical device applications.

PART B

Examining the consequences of calcium substitution on the structural and electrical properties of Y_3GaO_6

In the previous section, the effect of 2% alkaline earth metal (Ca^{2+}, Sr^{2+}, Ba^{2+}) doping on the A site of Y_3GaO_6 has been discussed. The above part illustrated that 2% Ca^{2+} ion substitution improves the bulk conductivity by more than three orders without any alteration in the conduction mechanism. However, the other dopants do not significantly enhance the conductivity because of the optimum dopant size mismatch between the dopant and the host ions.

Now in this section, we have studied the effect of substitution of higher concentrations of calcium doping, i.e. $x > 0.02$ in the system $Y_{3(1-x)}Ca_{3x}GaO_6$ ($x = 0, 0.02, 0.04, 0.08, 0.12$). The compounds, hereafter, referred as 0Ca, 2Ca, 4Ca, 8Ca and 12Ca, respectively for $x = 0.00, 0.02, 0.04, 0.08$, and 0.12. The structural, thermodynamical, optical, and electrical feature of these compositions is discussed below.

6.5 Results and Discussion

6.5.1 Structural Studies

Room temperature X-ray diffraction patterns of the calcium substituted tri-yttrium gallate $Y_{3(1-x)}Ca_{3x}GaO_6$ ($x = 0.00, 0.02, 0.04, 0.08, 0.12$) samples are shown in Figure 6.15. The undoped (i.e. 0Ca) and 2% of Ca doped sample (i.e. 2Ca) matches well with the orthorhombic structure of earlier reported Y_3GaO_6 having space group *Cmc2₁* and corroborated with ICSD No. 155086[113]. On further increase of the dopant concentration (x), secondary phases of

Y_2O_3 and $CaCO_3$ corresponding to ICSD No. 23811 and 186772, respectively, are observed. It can be seen that the intensity of the secondary peaks continuously increases for $x > 0.02$. This can also be observed that peaks get broaden with the increase of calcium concentration. The peak broadening (FWHM) relative to the most intense peak is shown in Table 6.5.

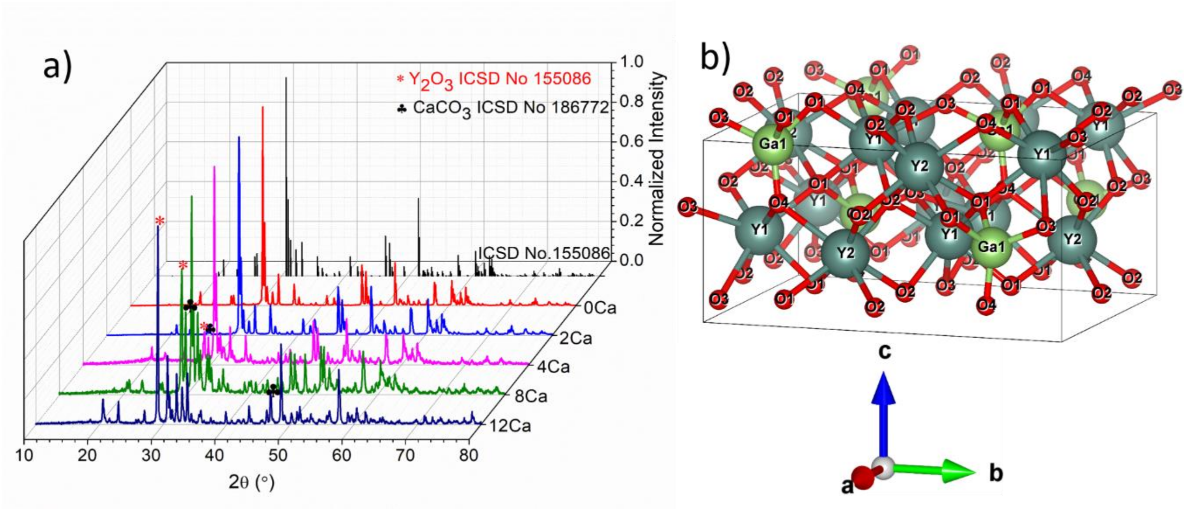

Figure 6.15. (a) XRD patterns of studied compositions **(b)** Crystal structure of Y_3GaO_6

To calculate the fraction of secondary phase, the phase purity of the samples were determined using the formulae $\phi_{purity} = \frac{I_p}{I_p+0.8I_s}$, where I_s, the maximum intensity of the secondary phase, and I_p is the maximum intensity of the primary phase [232][233]. The peaks corresponding to impurity phases are also indicated in Figure 6.15(a). The phase purity percentage are shown in Fig. 6.16. To examine the strain effect on the distortion of crystal structure, crystallite size and lattice strain are calculated using the Williamson Hall plot. The Williamson hall method is expressed by the formula $\beta cos\theta = \frac{K\lambda}{D} + 4\varepsilon sin\theta$, where β is the full-width half maxima at Bragg's angle 2θ, D is average crystallite size, K is shape factor, and ε is strain [234]. The calculated values of the various structural parameters are listed in Table

6.5. Almost negligible change in strain was observed for 2% of Ca doping, and thereafter, strain increases for higher doping concentration. It is attributed to the fact that Ca atoms are replacing the Y atom, and the size of the Ca (1.20Å) atom is slightly greater than Y (1.10Å) atom. So, at higher doping, it may lead to lattice expansion and also can enhance the lattice strain.

In order to interrogate the effect of doping on the crystal structure, Rietveld refinement was carried out using pseudo-Voight function profile, and it is shown in Fig. 6.17(a). Sample with x = 0.00 and 0.02 are well fitted with the single orthorhombic symmetry with space group $Cmc2_1$. However, samples with x > 0.02 could not be fitted using single orthorhombic symmetry. So, the refinement is done using three symmetry, i.e. orthorhombic ($Cmc2_1$) for Y_3GaO_6, cubic (*I a -3*) for Y_2O_3 and triclinic (*P -1*) for $CaCO_3$. The goodness of the fit lies within the appreciable range (listed in table 6.5). The refinement results illustrate the formation of impurity phases. For x > 0.02, there is a sharp increase in the secondary phases. So, it can be inferred that 2% is the solubility limit of the Ca doped Y_3GaO_6 system. For clear illustration of pure phase in x = 0.00 and 0.02 composition, full structure refinement of the composition is shown in Fig. 6.17 (b). Lattice parameters and volume corresponding to all the phases are estimated and plotted in Fig. 6.18 (a-c). Lattice expansion, along with volume expansion, is observed with the increase in Ca concentration. The lattice parameter increases first upto 2Ca, and then after decreases as the impurity phase dominates in the sample. It is usually observed that the lattice parameters of materials either decreases or increases with respect to the anionic or cationic vacancies in the lattice. Deshpande et al. and Wang et al. reported that the lattice parameters of nanoceria and $BaSrTiO_3$ increases due to the oxygen vacancy[235][236].

For the detection of oxygen concentration, we have employed the crystallographic information obtained from the refinement, and we have future confirmed this with EDX measurement also. The oxygen deficiency estimated from the refinement parameters of all the samples are shown in Fig. 6.18(d). It is observed that the oxygen deficiency increases with the increase in the Ca concentration because of the charge compensation mechanism. To analyze the oxide ion conduction pathways in the compositions, we investigated the bond valance energy landscapes (BVELs) for a test oxide ion O^{2-} using soft-BV software. The BVE of the test anion was calculated using the lattice parameters and position coordinates obtained from the Rietveld refinement data.

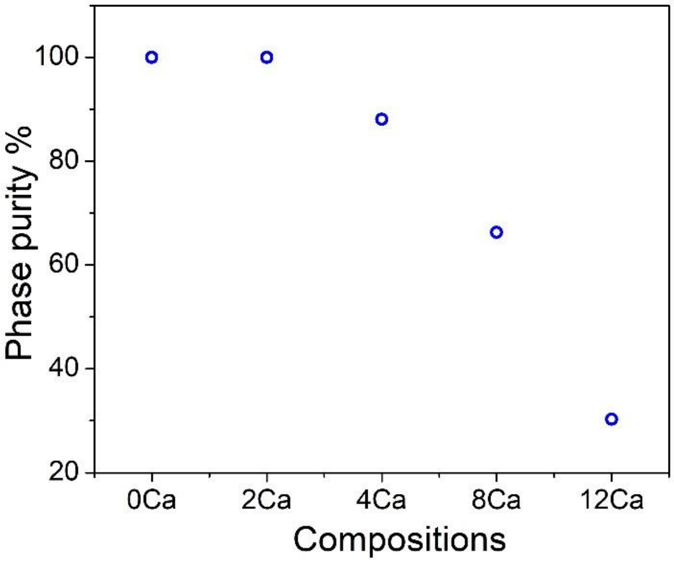

Figure 6.16: The percentage of phase purity with the increase in calcium concentration in Y_3GaO_6

Table 6.5: Crystallite size, lattice strain, density and FWHM of the studied samples

Sample Code	**Crystallite size (μm)**	**Lattice strain**	**Density (g/cm^3)**	**Porosity**	**FWHM (°)**	**Rietveld Bragg R factor**	**Parameters Rf factor**	**χ**
0Ca	1.60	$2.72 x10^{-04}$	3.8	0.300	0.114	3.05	2.40	4.24
2Ca	3.17	$2.70\ x10^{-0}$	5.3	0.024	0.163	8.19	5.51	7.72
4Ca	2.17	$5.35\ x10^{-0}$	4.8	0.116	0.140	13.8	18.2	11.0
8Ca	1.88	$6.86\ x10^{-0}$	4.7	0.134	0.147	18.0	24.8	22.9
12Ca	3.96	$1.44\ x10^{-03}$	4.3	0.208	0.145	17.8	25.1	21.9

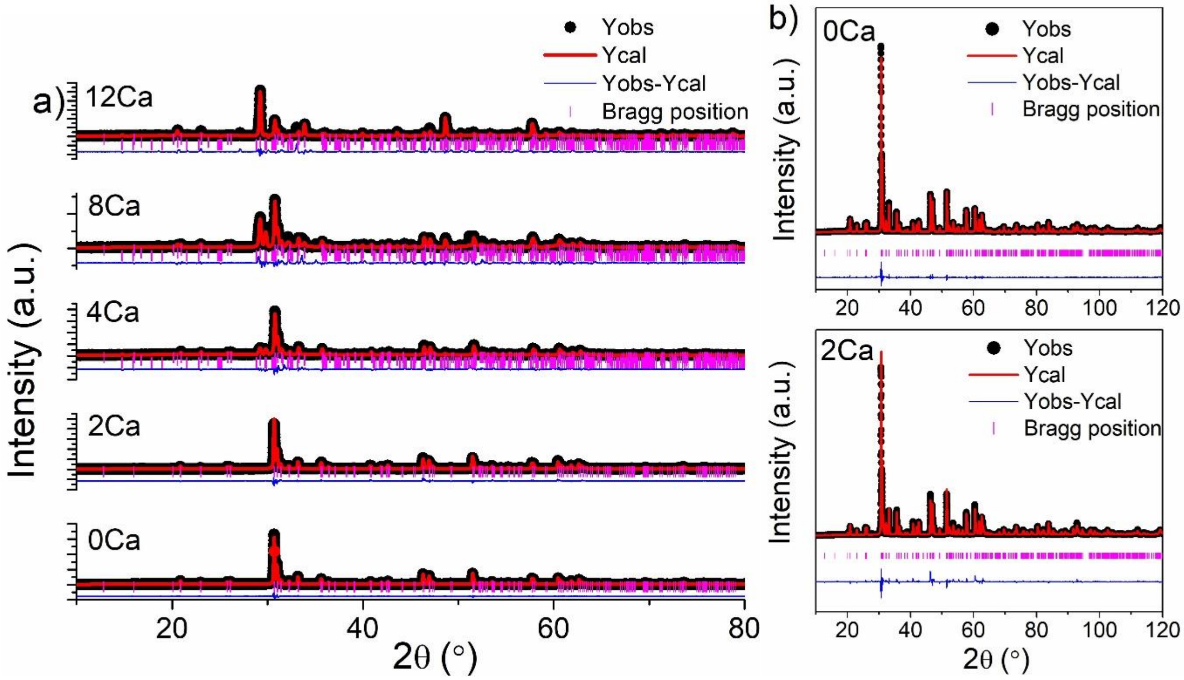

Figure 6.17: (a) Rietveld refinement fit pattern of all the studied systems **(b)** Full structure refinement of 0Ca and 2Ca composition. Black circles and red fit represent the experimental and calculated intensities. Magenta tick and blue line at the bottom represent Bragg position and difference profile between observed and calculated intensities

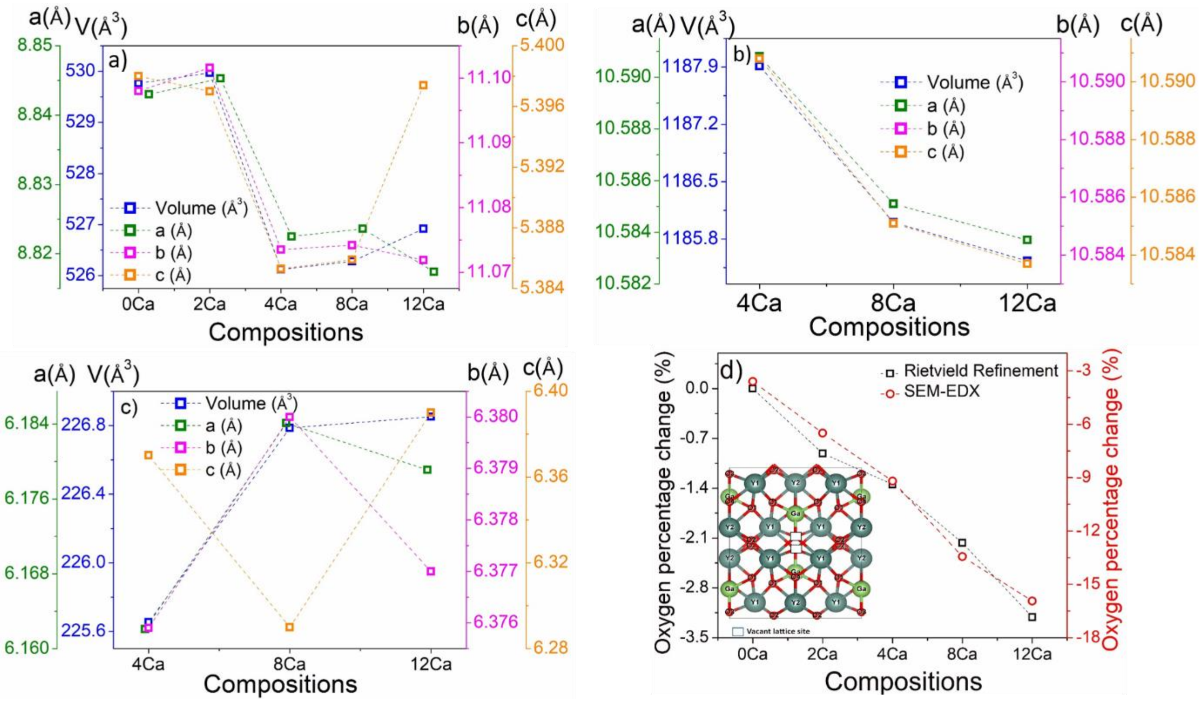

Figure 6.18: (a-c) Variation of lattice parameters and volume with dopant concentration for orthorhombic (Y_3GaO_6), cubic (Y_2O_3) and triclinic ($CaCO_3$) phases, respectively **(d)** Oxygen percentage change for all the compositions analyzed from Rietveld refinement and SEM-EDX studies. Inset in the figure showing the structure of 2Ca with vacant oxygens (□) at O3 site

6.5.2 Surface morphology and density

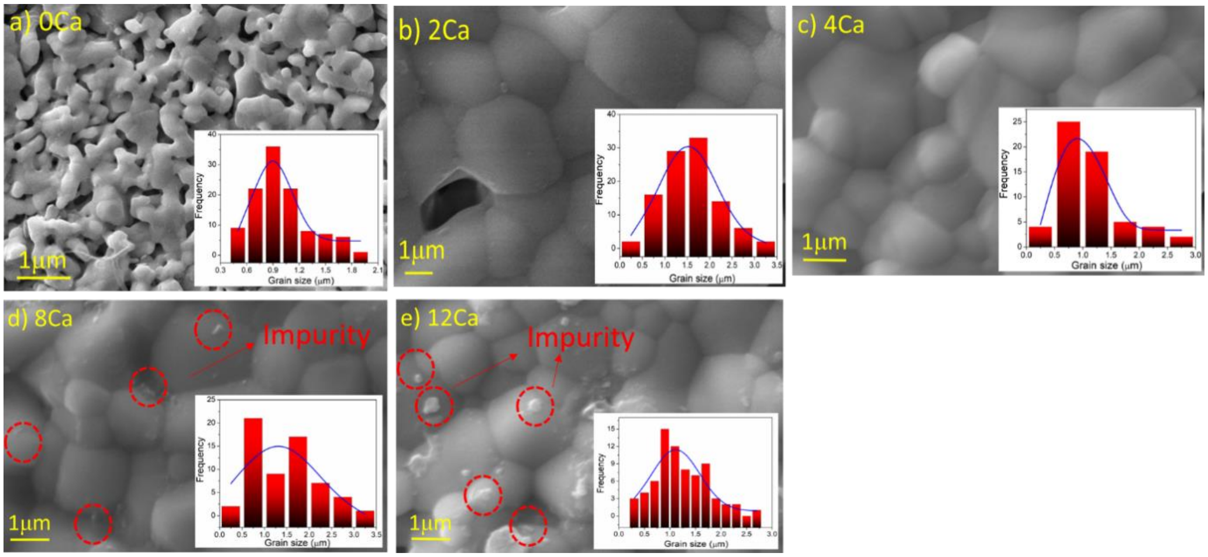

Figure 6.19: (a-e) SEM micrographs of $Y_{3(1-x)}Ca_{3x}GaO_6$ (x = 0, 0.02, 0.04, 0.08, 0.12) compositions. Inset shows grain size variation of respective samples. The dotted circles show Y_2O_3 and $CaCO_3$ impurities

The representative SEM micrographs for studied compositions are depicted in Fig. 6.19. The micrographs reveal the polycrystalline nature of the samples with well-defined grain and grain boundaries. These micrographs show the slightly porous behaviour for undoped (x = 0) and dense morphology for calcium doped (x = 0.02, 0.04, 0.08, 0.12) samples. For the composition with to x = 0.02, grains are well connected; however, further increase in the calcium concentration a few impurity phases (of Y_2O_3 and $CaCO_3$) are also observed (Fig. 6.19). The formation of the impurity phase retard the densification and grain size. The density of the compositions measured using the Archimedes Principle are listed in Table 6.5. The decrease in the density after the solid solubility limit (2%) argues the independent evolution of the secondary phases in the Y_3GaO_6 matrix.

6.5.3 UV-Vis Analysis

The energy band gap of all the studied compositions was calculated from extrapolating Tauc's plot, as shown in Fig. 6.20. The Wood and Tauc's relation is given by $\alpha h\upsilon = (h\upsilon - E_g)^n$, where α is the absorption coefficient, h is plank constant, υ is frequency, E_g is band gap, and n is associated with the type of transition [237]. Here, n = ½ corresponds to direct transition and n =2 corresponds to indirect transition. The estimated band gaps are shown in table 6.6. The estimated band gap for Y_3GaO_6 is 5.50 eV and agrees with the literature [238]. The band gap was found to decrease for the compositions with x = 0.02, 0.04, 0.08, 0.12. The band gap is lowest for 2% Ca doped sample and thereafter increases with further increase in doping concentration. This widening in the band gap at higher doping concentration may be attributed to two reasons: (1) Band tailing; because of impurity distribution [239] (2) Moss–Burstein effect; occurs when the charge carrier concentration exceeds the conduction edge density of states [240].

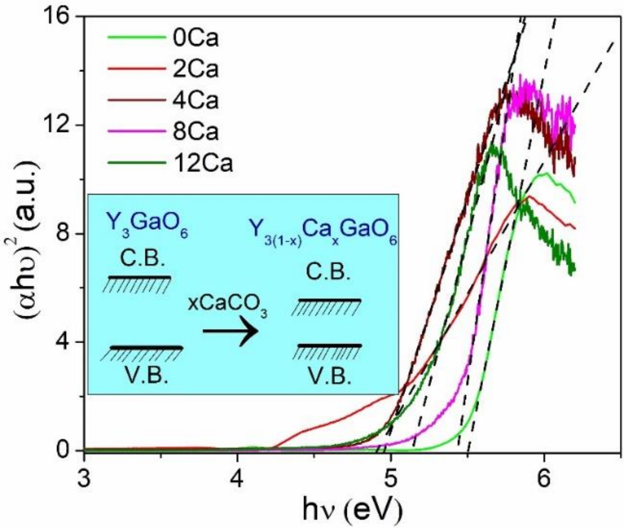

Table 6.6: Energyband gap

Composition	Band-gap E_g (eV)
0Ca	5.50
2Ca	4.91
4Ca	4.96
8Ca	5.44
12Ca	5.14

Figure 6.20. Tauc plot showing the variation of $(\alpha h\upsilon)^2$ vs hυ with dopant concentration

6.5.4 Impedance Analysis

The Nyquist plot (Z' vs Z") of all the synthesized compositions at 700 ºC are depicted in Fig. 6.21(a). It is observed that there is one large depressed semi-circle followed by a small depressed semi-circle in the plot. At 700 ºC undoped Y_3GaO_6 sample exhibits large resistive region, and after doping with calcium, this resistive region is found to decrease and is shown in the inset of Fig. 6.21(a). Total resistance R (= R_g+R_{gb}) is found to be minimum for 2Ca. The grain and grain-boundary resistance can be determined using fitting of depressed semi-circular Cole-Cole plot and taking resistive intercept on X-axis. The total conductivity is given by $\sigma_{total} = \frac{t}{A\times(R_g+R_{gb})}$, where t is the thickness, R_g is grain resistance, R_{gb} is grain boundary resistance, and A is the circular area of the pellet. Figure 6.21(b) depicts the Arrhenius plot of studied compositions described by the equation:

$$\sigma T = \sigma_0 \exp\left(\frac{-E_a}{k_B T}\right) \quad (6.9)$$

where *T* is temperature, E_a is the activation energy, σ_0 is the pre-exponential factor, and k_B is the Boltzmann's constant [212][242]. At first sight, it is observed that undoped Y_3GaO_6 exhibits lower conductivity compared with the doped materials. Indeed, the conductivity increases only for 2% of calcium doping, and then after, it decreases for higher doping concentration, possibly due to the segregation of impurities at grain boundaries. When the divalent Ca^{2+} is introduced in the lattice to replace Y^{3+} then more number of oxygen vacancies is introduced inside the crystal, and this can be understood with the following Kroger-Vink equation:

$$xCaCO_3 \xrightarrow{1/3Y_{3(1-x)}GaO_6} xCa_Y' + O_O^X + V_O^{\cdot\cdot} + xCO_2 \qquad (6.10)$$

Aliovalent doping is considered as the source of vacancies by charge compensation mechanism. It is further supported by the Photoluminescence studies of the system. In order to achieve a higher order of oxide-ion conductivity, the material must have higher number of oxygen vacancies to facilitate the motion of charge carriers. As calcium doping increases, the increase in the grain-boundary conductivity is much higher as compared to that of the grain. It is also a well-known fact that since the grain-boundary forms a continuous path for oxide ion migration, so the total conductivity σ_{total} varies in the same way as R_{gb}. But in this case, at higher doping concentrations (> 2% of Ca), a few impurity phases were found to segregate along the grain-boundaries that restrict the conduction process along the grain-boundaries.

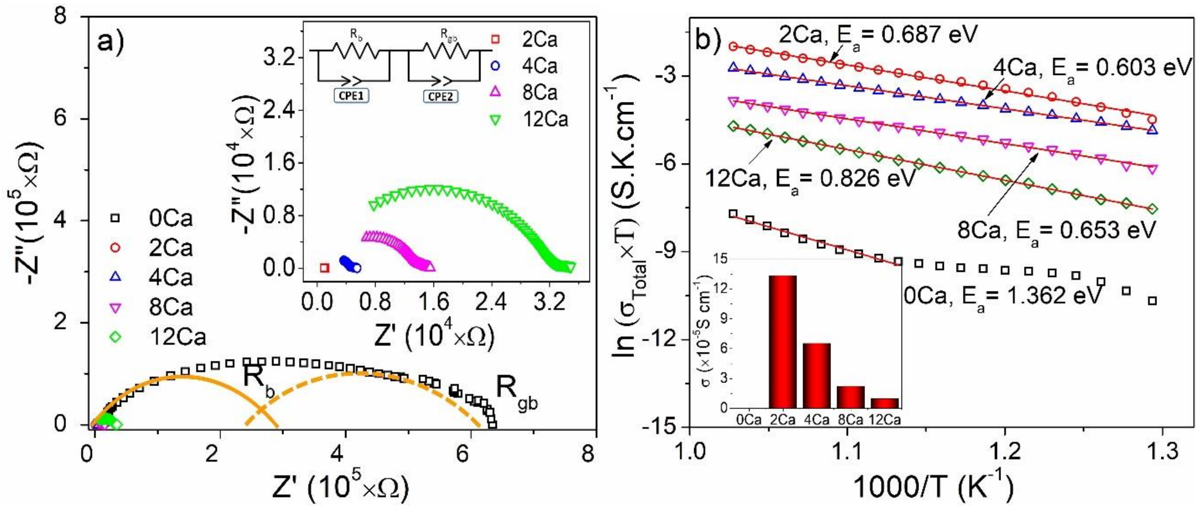

Figure 6.21: (a) Impedance Nyquist plot at 700 ºC. Inset depicts the equivalent circuit to fit the impedance spectra along with impedance plot of Ca doped compositions **(b)** Arrhenius plot for total conductivity of studied compositions. Inset depicts the conductivity histogram at 700 ºC

Figure 6.22 (a-b) depicts the Arrhenius plot of grain and grain-boundary conductivity. These plots were found almost linear in the entire measurement range. This curve demonstrated that the increase in the grain-boundary conductivity is higher than that of grain with doping. The activation energies corresponding to both grain and grain-boundary are calculated and listed in Table 6.7. The value of activation energy suggests that conduction is mainly due to the migration of oxygen vacancies. It is observed from table 6.7 that 2Ca possesses maximum conductivity and makes it a relevant candidate for electrolyte application in SOFCs. Conductivity further decreases with an increase in *x* due to the segregation of unreacted Y_2O_3 and $CaCO_3$ phases in the grain-boundary and reducing oxygen vacancy migration. It was further confirmed in the VSEPR studies.

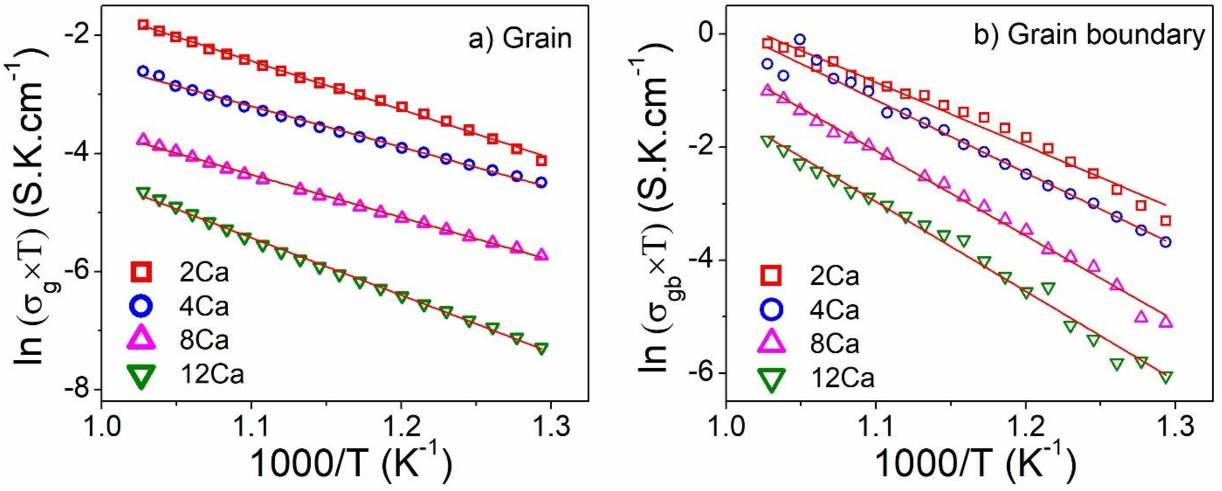

Figure 6.22: Arrhenius plot for **(a)** grain **(b)** grain-boundary conductivity of studied compositions

Table 6.7: Comparison of grain, grain-boundary conductivity and activation energy of Ca doped samples

Sample	σ_{grain} (S.cm^{-1}) (700 ˚C)	$\sigma_{grain-boundary}$ (S.cm^{-1}) (700 ˚C)	Activation Energy Grain (eV)	Activation Energy Grain-Boundary (eV)
2Ca	$1.663\text{x}10^{-4}$	$8.708\ \text{x}10^{-4}$	0.632	0.795
4Ca	$7.595\ \text{x}10^{-5}$	$6.060\ \text{x}10^{-4}$	0.518	1.031
8Ca	$2.352\ \text{x}10^{-5}$	$3.742\ \text{x}10^{-4}$	0.548	1.219
12Ca	$9.868\ \text{x}10^{-6}$	$1.580\ \text{x}10^{-4}$	0.760	1.287

6.5.5 Electron density map

To correlate the conductivity data with the structure, ion-conducting channels were analyzed. Figure 6.23 depicts the formation of ion channels using valence shell electron repulsion theory (VSEPR theory) after Rietveld refinement of the X-ray data for the studied samples in the z-y plane. It shows the formation of ion channels where the electron density is minimum. For the undoped Y_3GaO_6 sample and 2% Ca doped sample (i.e. 0Ca and 2Ca), multi-directional channels are available for the movement of oxide ions. Moreover, with the further increase in the Ca concentration, new scattering centres are introduced because of the presence of impurity phases. This leads to the impasse of paths of oxide ion migration resulted in the decrease in ionic conductivity. This is corroborated with the conductivity study of investigated compositions.

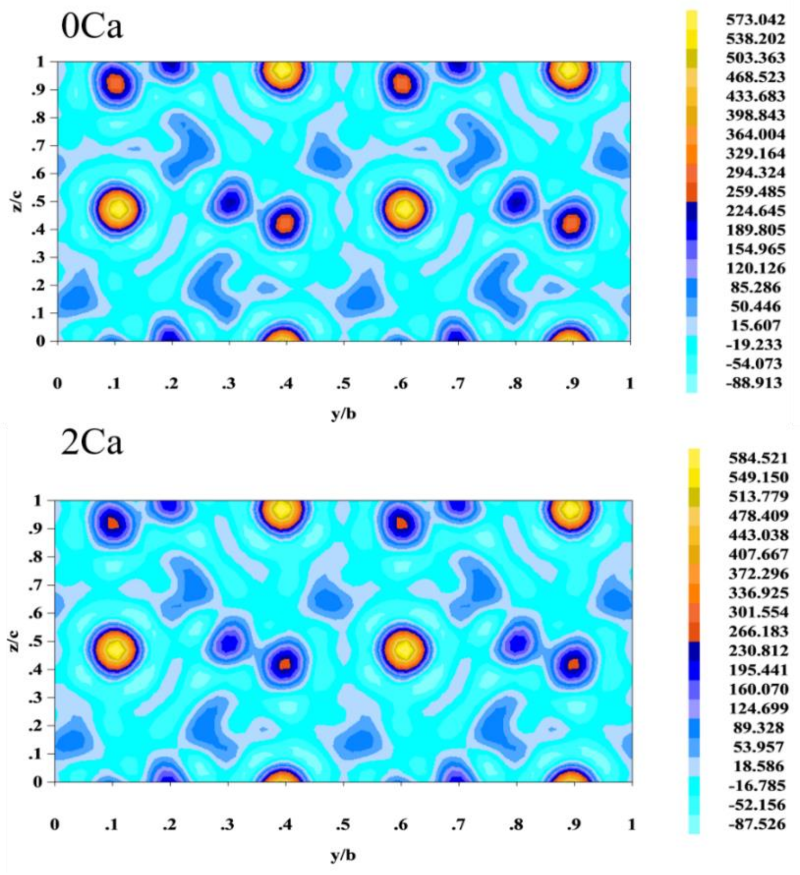

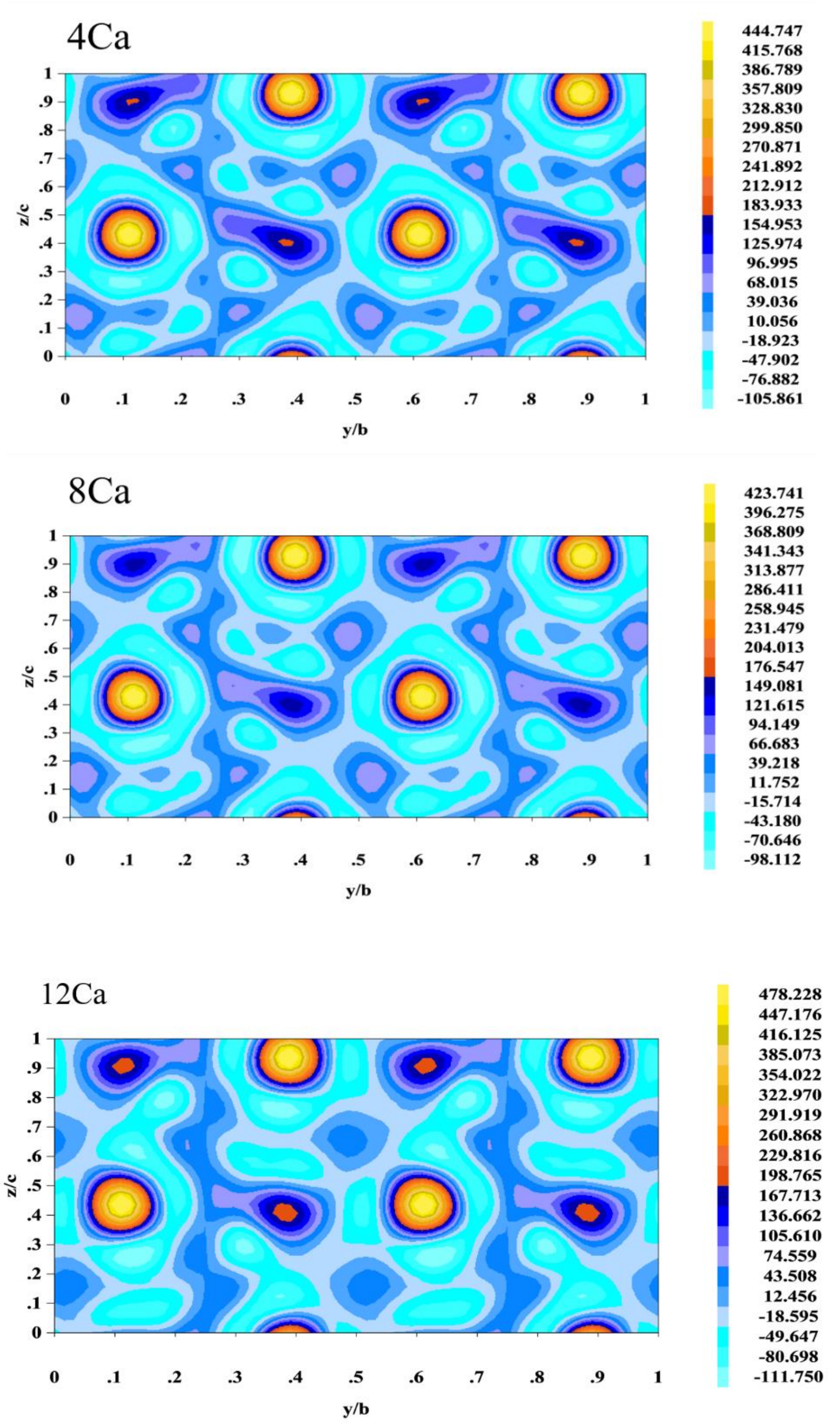

Figure 6.23: Electron density contour map of all studied compositions in the z-y plane

Further, to check the ionic contribution of the specimens, the conductivity data were fitted with the space charge ionic model. Figure 6.24 depicts the space charge ionic model fitting for the studied specimens [242]. The fitting parameter χ^2 ~ 0.99 for all the samples suggested the ionic conduction in the samples.

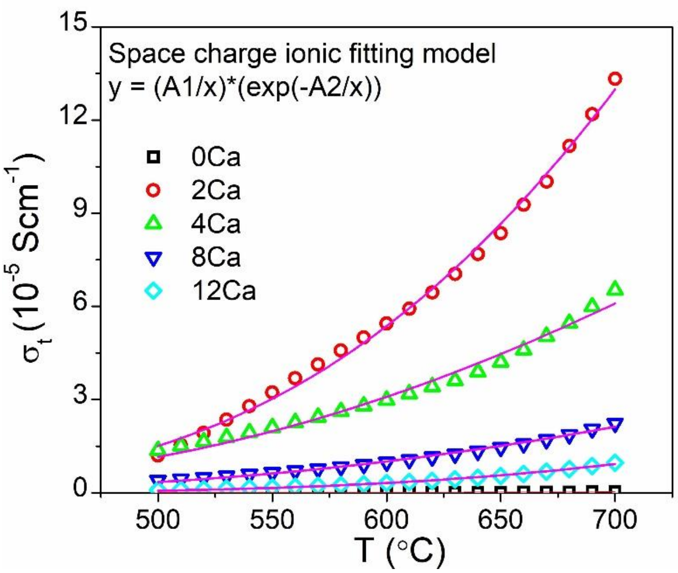

Figure 6.24: Space charge ionic fitting model for all the studied specimens

6.5.6 PL Analysis

Room-temperature photoluminescence (PL) spectra of the studied composition in the energy range of 2-4 eV are shown in Fig. 6.25. The doping of Ca on the Y-site does not show any significant influence on the peak position rather; it varies only the peak intensity. Our earlier report on this material says that doping in Y_3GaO_6 with aliovalent substitution generates defect levels[243]. Calcium ion (Ca^{2+}) modifies the defect chemistry of Y_3GaO_6, which is clearly observed in figure 6.23. On calcium doping, Ca^{2+} ions will drift inside the system and can occupy the Y site. The ionic radii mismatch and charge balance arising due to this can lead to the formation of defects [244]. These defects will suppress the radiative transition and decrease the PL intensity. Upon increasing the calcium concentration, the distortion rises, leading to the surge of defect sites in Y_3GaO_6, suppressing the PL intensity. Usually, the lower

PL intensity corresponds to higher conductivity because of the smaller effective charge carrier separation and lower recombination rate.

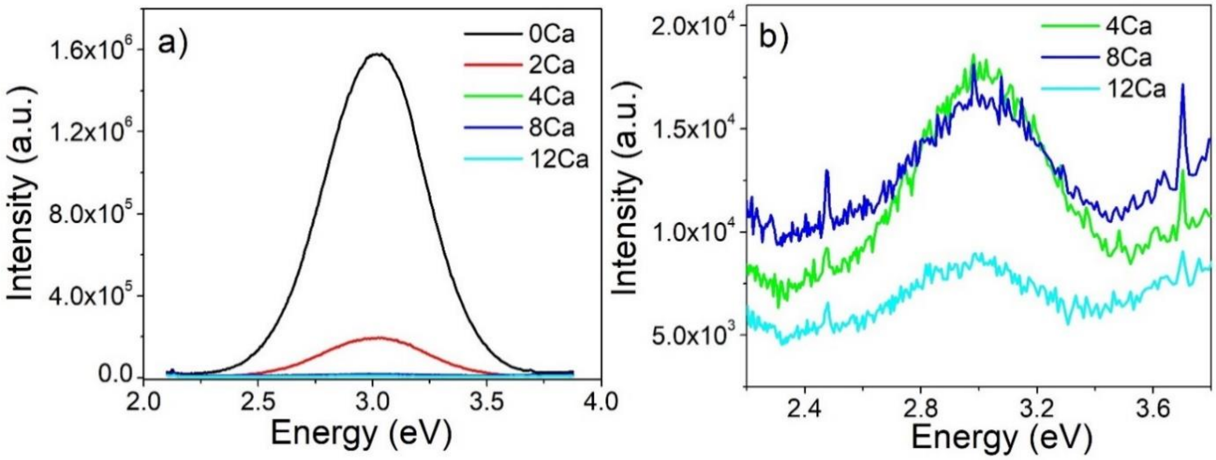

Figure 6.25: (a-b) Room temperature photoluminescence spectra with an excitation wavelength of 305 nm

6.5.7 Scaling behaviour and conduction mechanism

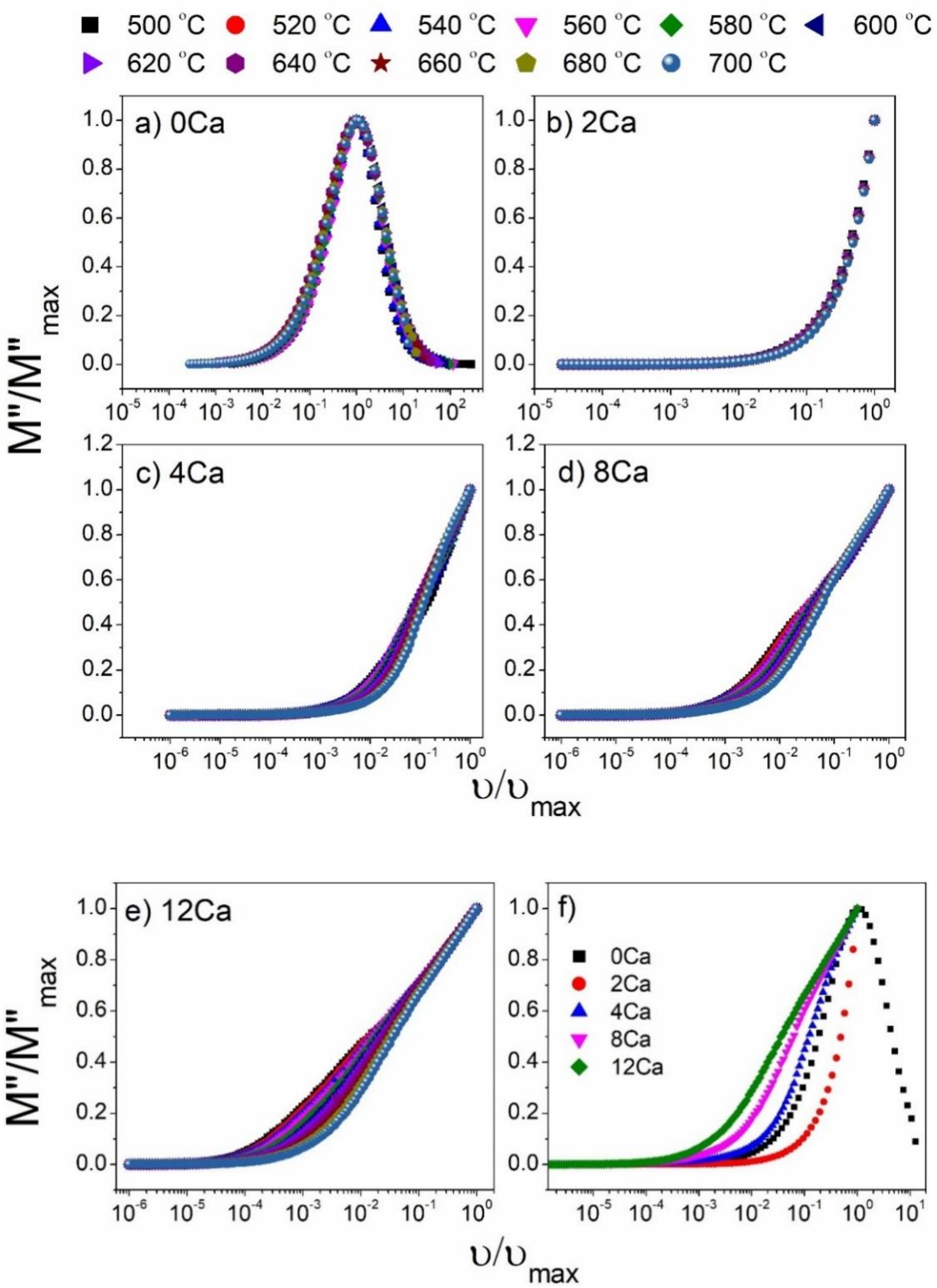

Figure 6.26: Modulus scaling behaviour for all the samples at different temperatures

In order to gain an idea about relaxation dynamics, the scaling behaviour of modulus spectra has been studied. Representative Modulus master curve for 0Ca, 2Ca, 4Ca, 8Ca and 12Ca samples at different temperatures are shown in Fig 6.26 (a-e). Here imaginary part of modulus has been scaled by the maximum value of M (i.e. M″), and the frequency axis is scaled by the maximum value of ʋ (i.e. ʋ″). The superposition of all the spectra into a master curve at various temperatures for the 0Ca and 2Ca samples shows the temperature-independent behaviour of the dynamical process. Whereas dispersion in the master curve for 4Ca, 8Ca and 12Ca suggest temperature-dependent relaxation dynamical behaviour. Fig 6.26 (f) shows the dispersion of modulus spectra for different samples at 700 °C. This dispersion in the scaled modulus spectra with different compositions shows the absence of time-temperature superposition behaviour, i.e. with the change in the temperature, not only the number of charge carrier changes but also the conduction mechanism. This also results in the deviation of conduction pathways for all the samples.

6.5.8 Cyclic Voltammetry

Electrochemical responses of undoped (0Ca) and 2Ca samples in aqueous 1M NaOH solution at room temperature are shown in Fig. 6.27. The cyclic voltammogram depicted in the figure was studied in the sweep potential range of -1.5 to 1.5 V and scan rate of 30, 50, 100, 150, 200 & 250 mV/s. It was observed that the value of current increases with the increase in the scan rate. The area of the curve also increases with the increase in the sweep rate. The current density was higher for 0Ca as compared to 2Ca for the same scan rate. For 0Ca, significant oxidation and reduction peaks are observed, whereas, for 2Ca, no such peaks are observed. It suggests that the electrodic response of 0Ca is more than 2Ca[245]. Specific capacitance Cs of the material was calculated using Cs = 1/mS × (area of integration) equation, where m is the mass of material deposited, and S is the scan rate. Its value is plotted in Fig. 6.27(c). The obtained maximum capacitance value is 450 F/g for 0Ca and 17 F/g for 2Ca. This high capacitance in Y_3GaO_6 is mainly attributed to its morphology and porous nature. High capacitance value makes it suitable for energy storage applications. The decrement in the capacitance of 2Ca is primarily because of the decrease in porosity, as the decrease in the porosity makes the movement of ions difficult. These electrochemical results suggest that undoped Y_3GaO_6 may be a possible candidate for pseudo-capacitors.

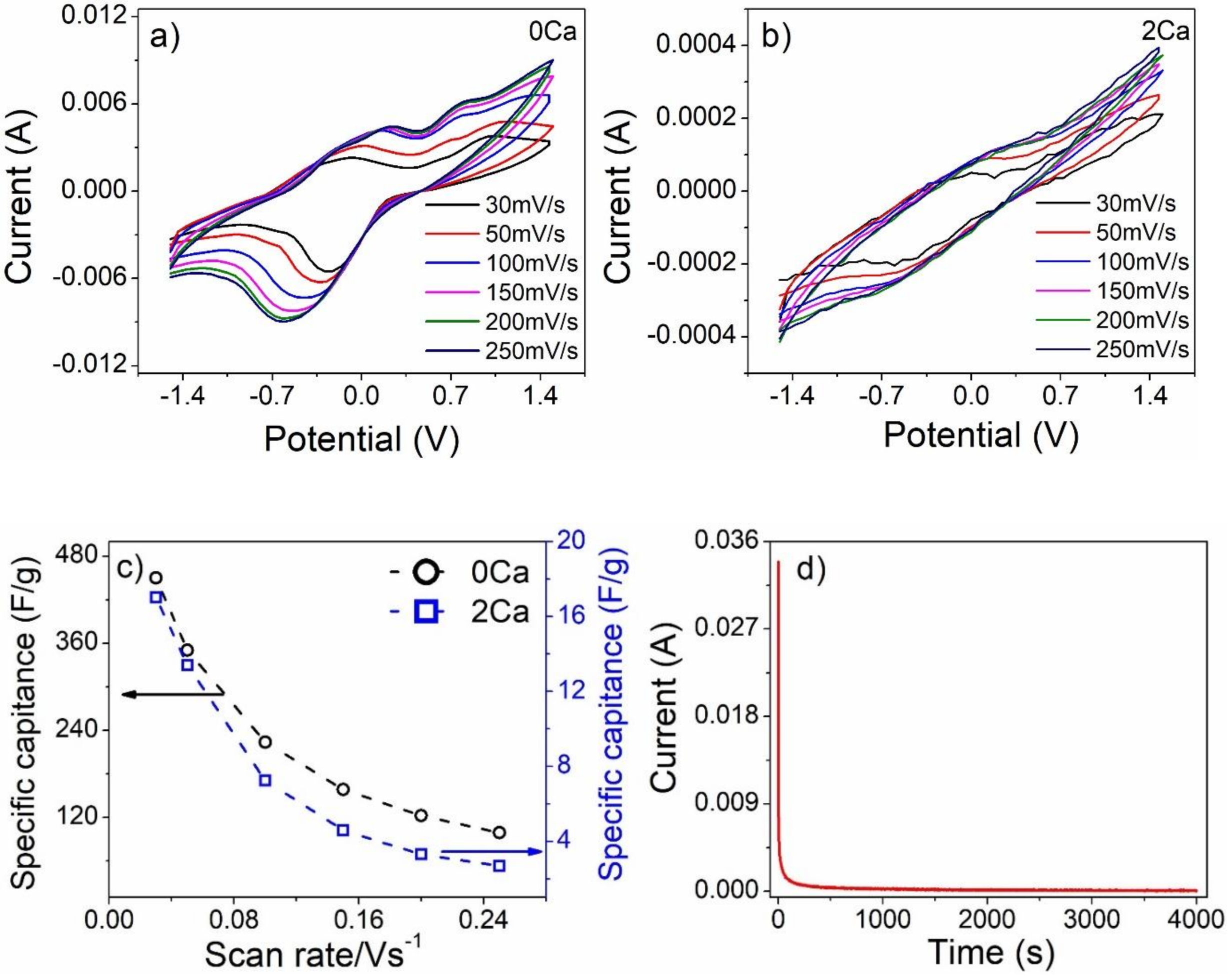

Figure 6.27: (a-b) Cyclic voltammogram curve with the various scan rate **(c)** Specific capacitance at different scan rates for 0Ca and 2Ca sample **(d)** Chronoamperometryplotof undoped Y_3GaO_6 sample at 1.5 V

At lower scan rate, the electrolyte ions get sufficient time to penetrate the pores of the material, while at higher scan rate, it only accumulates on the outer surface. Therefore, with the increase in the scan rate, specific capacitance decreases. Figure 6.27(d) shows the Chronoamperometry plot of undoped Y_3GaO_6 sample at 1.5 V. Chronoamperometry measurement of the samples was carried out to examine the stability of Y_3GaO_6 sample in 1M NaOH solution. It was done at a holding potential of 1.5 V for 4000 sec, and the value of current was recorded as the function of time. The peak current was high at the initial stage, and the sharp current drop was observed in little time ($t < 8$ sec). These results support the stability of the material in the investigated electrolyte.

6.6 Conclusions

Structural and electrical properties of undoped and Ca doped Y_3GaO_6 system was meticulously analyzed and discussed. These specimens were found to exhibit orthorhombic symmetry comprising the space group $Cmc2_1$. A few secondary phases of Y_2O_3 and $CaCO_3$ were also observed for higher dopant concentration (> 2% of Ca). In the UV-vis study, the minimum band gap was found for 2% Ca doped Y_3GaO_6, indicating the leeway of ease conduction in this composition as compared to other dopant concentrations. The ionic conduction was expected in the photoluminescence study of the doped Y_3GaO_6 system, which also corroborates with the experimental findings. Scanning electron microscopy reveals that dense grain morphology for doped samples. Impedance spectroscopy measurement reveals that initially, grain boundaries are facilitating the conduction process, but at higher concentrations of Ca it becomes resistive because of segregation of secondary impurity phases along the grain boundaries. With the Ca substitution, density increases along with the change in morphology.

A large number of oxygen vacancy generated in the grain boundary and significant variation in the density is possibly responsible for the high conductivity at room and higher temperatures. Modulus spectroscopy studies were also employed to analyze the conduction mechanism and to support the experimental findings. Cyclic voltammetry results evinced that undoped Y_3GaO_6 may have exhibited pseudo-supercapacitive characteristics.